Title

Sedimentary response of a structural estuary to Holocene coseismic subsidence

Journal

Geological Society of America Bulletin, 134(7-8)

ISSN

0016-7606

Authors

Reynolds, Laura C

Simms, Alexander R

Rockwell, Thomas K

et al.

Publication Date

2022-07-01

DOI

10.1130/b35827.1

Peer reviewed

Sedimentary response of a structural estuary to Holocene coseismic subsidence

Laura C. Reynolds[1,5], Alexander R. Simms[1], Thomas K. Rockwell[2], Yusuke Yokoyama[3], Yosuke Miyairi[3], Alexandra Hangsterfer[4]

[1]University of California Santa Barbara, Department of Earth Science, 1006 Webb Hall, University of California, Santa Barbara, CA 93106

[2]San Diego State University, Department of Geological Sciences, MC-1020, 5500 Campanile Dr., San Diego State University, San Diego, CA 92182-1020

[3]The University of Tokyo, Atmospheric and Ocean Research Institute, 5-1-5, Kashiwanoha, Kashiwa-shi, Chiba 277-8564 Japan

[4]Scripps Institution of Oceanography, 9500 Gilman Drive, La Jolla, California 92093

[5]Worcester State University, Department of Earth, Environment, and Physics, 486 Chandler St. Worcester, MA 01602

ABSTRACT

Stratigraphic evidence for coseismic subsidence has been documented in active-margin estuaries throughout the world. Most of these studies have been conducted in subduction zone or strike-slip settings; however, the stratigraphic response to coseismic subsidence in other tectonic and climatic settings remains understudied. Here we show evidence for late Holocene coseismic subsidence in a structural estuary in southern California, a Mediterranean climate region. Below the modern marsh surface, an organic-rich mud containing marsh gastropods, foraminifera and geochemical signatures indicative of terrestrial influence (mud facies) is sharply overlain by a blue-gray sand containing intertidal and subtidal bivalves and geochemical signatures of marine

influence (grey sand facies). We use well-established criteria to interpret this contact as representing an abrupt 1.3 ± 1.1 m rise in relative sea level (RSL) generated by coseismic subsidence with some contribution from sediment compaction and/or erosion. The contact dates to 1.0 ± 0.3 ka and is the only event indicative of rapid RSL rise present in the 7 kyr sedimentary record studied. Consistent with observations made in previous coseismic subsidence studies, an acceleration in tidal-flat sedimentation followed this abrupt increase in accommodation; however, the recovery of the estuary to its pre-subsidence elevations was spatially variable and required 500-900 years, longer than the recovery time estimated for estuaries with larger tidal ranges and wetter climates.

INTRODUCTION

Evidence for individual coseismic subsidence events has been extensively demonstrated in tectonically active coastal regions throughout the world by the presence of marsh surfaces buried by intertidal sediments due to deformation from subduction zone earthquakes (Atwater, 1987; Atwater and Hemphill-Haley, 1997; Atwater et al., 2001; Hawkes et al., 2011; Reinhardt et al., 2010) and strike-slip earthquakes (Clark et al., 2013; Cochran et al., 2017; Knudsen et al., 2002). Localized coseismic subsidence related to movement along upper crustal structures has also been inferred for a variety of tectonic regimes (Bourgeois and Johnson, 2001; Cundy et al., 2000; McNeill et al., 1999; Pratt et al., 2015; Sherrod, 2001) and is the likely cause of subsidence documented in fault-bounded, structurally-controlled estuaries outside the direct influence of subduction or strike-slip earthquakes (Cundy et al., 2000; Simms et al., 2016). Determining recurrence and magnitudes of coseismic subsidence is necessary to assess seismic hazards and can elucidate subsurface relationships among structures in complex tectonic regions (i.e., Shennan et al., 2016). However, differentiating the effects of coseismic subsidence from

nonseismic processes that produce similar stratigraphic changes, such as floods, global mean sea-level rise, sediment flux-driven transgressions, local morphological changes (barrier breaching, mouth migration), or anthropogenic-induced subsidence, is difficult (Shennan et al., 2016), especially where subsidence is localized (i.e., within a structural estuary) rather than regional (i.e., megathrust-related crustal deformation).

Previous studies (Nelson et al., 1998; Nelson et al., 1996; Shennan et al., 2016) have developed criteria for recognizing coseismic subsidence in the stratigraphic record, based mainly on observations from subduction zone earthquakes. These criteria include, but are not limited to, the following: a laterally extensive and sharp contact; evidence for a sudden RSL rise; and evidence for synchronicity of change, replicated in multiple cores. These characteristics are interpreted to represent the estuarine response to a sudden decrease in elevation, i.e., an rise in relative sea level (RSL).

While identification of subsidence in the sedimentary record is important for hazard assessment, it is also important to understand the completeness and limitations of estuarine sediments as recorders of seismic events (Atwater et al., 2001; Dura et al., 2016). Previous work has shown that the tidal range (Atwater et al., 2001), sediment supply and source (Darienzo and Peterson, 1990), and patterns of relative sea-level change (Dura et al., 2016) all influence the response of estuarine environments to vertical displacement and therefore their ability to stratigraphically record coseismic events. However, the variability in estuarine response to coseismic subsidence within these different contexts, i.e., how this variability is characterized in the stratigraphic record, has received relatively little attention.

Here we use sediment cores and relative sea-level indicators from Carpinteria Marsh, a small structural estuary in southern California, and show stratigraphic evidence for an abrupt

environmental change that emplaced blue-grey sands on top of organic-rich, fine-grained muds throughout the marsh. We hypothesize that the contact represents an abrupt rise in relative sea level caused by coseismic subsidence along a local thrust fault. Using multi-proxy sea level indicators and a robust chronology, we test whether the nature of this contact is consistent with the criteria developed to identify coseismic subsidence in the stratigraphic record and discuss its potential hazard and structural implications. We show that traditional criteria used to identify coseismic deformation events remain applicable for recognizing coseismic subsidence even when the subsidence appears to be highly localized within a structural estuary; however, the non-tectonic characteristics of the environment (tidal range, sediment supply, climatic context) must be carefully considered to differentiate coseismic events from other processes in these dynamic systems.

STUDY AREA

The study area, Carpinteria Marsh (34^{o} 24’ N 119^{o} 31’ 30” W), is located along the Santa Barbara Channel in southern California, USA. The marsh lies within the axis of the Carpinteria basin, a small, faulted syncline (Jackson and Yeats, 1982) (Fig. 1c) on the down-thrown side of the south-dipping, out-of-syncline (Mitra, 2002) Rincon Creek Fault (RCF) (Jackson and Yeats, 1982). Carpinteria basin lies on the southern flank of the Santa Ynez Mountains (Fig. 1), which are part of the Western Transverse Ranges, a large east-west trending fold and thrust belt that has exhibited rapid uplift since the Pliocene resulting from compression due to a restraining bend in the San Andreas fault system (Jackson and Yeats, 1982; Rockwell et al., 2016). Large north-dipping thrust faults in Ventura and Santa Barbara counties, such as the Pitas Point-Ventura Fault (Fig. 1), may have the potential for Mw 7.5-8 earthquakes (Levy et al., 2019; Rockwell et al., 2016). However, the subsurface geometry, and therefore the extent of the regional seismic

hazard, in the Ventura region is subject to ongoing debate (Hubbard et al., 2014; Jackson and Yeats, 1982; Johnson et al., 2017; Levy et al., 2019; Marshall et al., 2017; Rockwell et al., 2016); therefore, additional sedimentary records of seismic activity in the region may help clarify these interpretations.

Carpinteria marsh is a fragment of a once larger estuary that prehistorically occupied much of the low-lying coastal plain of the Carpinteria basin (Ferren, 1985). The marsh is dominated by Salicornia virginica, marsh pickleweed (Hubbard, 1996; Page, 1995; Sadro et al., 2007), and receives tidal flow through an inlet stabilized with a rock revetment in 1964 (Ferren, 1985) and freshwater input from two tidal creeks (Santa Monica and Franklin creeks) that enter the marsh's northeastern corner. The marsh has a tidal range of 1.01 m (Sadro et al., 2007), with high tide levels similar to those of the open coast, but truncated low water levels due to a lagged ebb tide from inlet constriction (Hubbard, 1996). Similar to observations in other salt marshes in California (i.e., (Thorne et al., 2018)), the vegetated marsh platform and mudflats range from mean low water (MLW) to elevations above mean higher high water (MHHW). The marsh is located in a Mediterranean climate region, characterized by mild, wet winters and warm, dry summers (Bakker and Slack, 1984); most of the small streams that run from the mountains to the coast only flow and transport sediments during storm events. Historically, three to five freshwater streams built alluvial fans into the fringes of the marsh during storm events but today the two remaining streams are channelized upstream from the marsh. One historical alluvial fan, attributed to a flood in 1914, is still visible in the northeastern corner of the marsh (Fig. 2) (Ferren, 1985).

METHODS

From 2012-2018, we collected 44 vibracores that sampled from 1 to 4 m below ground surface and five Geoprobe 7822DT cores that sampled up to 14 m below ground surface in Carpinteria Marsh (Fig. 1 and Supplemental Fig. S1, S2, S3) and established sedimentary facies using grain size, color, sedimentary structures, organic content, and foraminifera and shell taxonomy (Table 1). Core locations were determined with a TopCon Hyperlite + differential GPS or a handheld GPS; core-top elevations were determined with the differential GPS or Lidar corrected for vegetation error (Sadro et al., 2007). Elevations were corrected to NAVD88 using the online NOAA OPUS site (www.ngs.noaa.gov/OPUS/elevations). The vertical uncertainty for the ground surface elevation for all cores is less than 0.15 m. Sixty-eight organic, charcoal, and shell samples were used for radiocarbon analysis at the University of California Irvine Keck Carbon Cycle AMS Laboratory, while 26 samples were analyzed at the Atmospheric and Ocean Research Institute (AORI), The University of Tokyo (Yokoyama et al., 2010) (Table 2).

Thirty modern sediment samples collected from a transect along the marsh surface (see Supplemental Materials 1, Fig. S4) and 175 sediment samples from core CM46 were freeze-dried, crushed, and treated with 3 N HCl at 100 °C to remove inorganic carbon in preparation for carbon isotope analyses. A Delta V Advantage and Flash 2000 EA IRMS at AORI was used for isotopic analysis. Data were corrected for machine drift and amount-dependent deviations when necessary. Repeated analyses of internal standards indicated a 2σ uncertainty of 0.86‰. Core CM46 was scanned at 0.2 mm resolution on an Avaatech X-Ray Fluorescence (XRF) core-scanner at Scripps Institution of Oceanography at 10, 30, and 50 keV, which measured a suite of 29 elements. X-ray spectra were processed following Addison et al. (2013) and log ratios of elemental counts were used in interpretations because log ratios are less affected by variations in

the physical characteristics of sediments (water content, grain size, etc.) (Addison et al., 2013; Weltje and Tjallingii, 2008).

RESULTS

Facies descriptions and interpretations

We follow Reynolds et al., 2018 in their designation of four sedimentary facies present in Carpinteria Marsh: grey sand facies, brown sand facies, mud facies, and white sand facies. These facies are described in detail in Reynolds et al., 2018, but we summarize their characteristics here, as well as in Table 1. Deposits of white sand facies are localized to the upper meter of sediments throughout Carpinteria marsh and were previously interpreted to represent a historical washover event (Reynolds et al., 2018); therefore, we do not discuss this facies further in this paper.

The grey sand facies is shell rich, grey in color, fine to medium sand with silt-sand laminations, likely indicative of tidal influence, and is often massive or mottled. Grey sand facies deposits are devoid of foraminifera and ostracods, similar to modern beach and dune sand in Carpinteria (Wilson et al., 2014). However, the grey sand facies deposits contain articulated and fragmented shells of intertidal and subtidal bivalves (*Mascoma nasuta, Chione undulata, Leukoma staminea, Tagelus californianus, Saxidomus nuttalli, Ostrea spp., Leukoma laciniate, Cryptomya californica*). Therefore, we interpret the grey sand facies to represent a lower intertidal to subtidal depositional environment.

The mud facies is characterized by fine-grained organic-rich laminated and bioturbated mud and silt deposits. Mud facies deposits contain foraminifera species indicative of a marsh environment (*Miliammina fusca, Trochammina inflata, Elphidium excavatum, Jadammina macrescens* (Avnaim-Katav et al., 2017; Bentz, 2016; Scott et al., 2011) and shells of *Cerithidea*

californica, a mudflat/marsh gastropod (Sousa, 1983). This invertebrate assemblage is consistent with an intertidal mudflat/marsh environment.

The brown sand facies is characterized by fine to coarse sand beds, which are massive or normally graded. Beds of this facies often have sharp or erosional bases and contain ripple cross laminations or parallel laminations. The deposits are lithic-rich, brown in color, and are more common and thicker in the landward portions of the marsh. They lack shell material, except for the occasional *C. californica* fragment. We interpret the brown sand facies to represent storm derived flood deposits transported from the small streams draining into the marsh into an alluvial fan depositional environment at intertidal to supratidal elevations.

Stratigraphy and evidence for environmental change

At the base of all cores that penetrate below 10 m NAVD88 is a bed of grey sand facies, which grades upwards into beds of mud facies, interbedded with beds of brown sand facies (Fig. 3) (Simms et al., 2016). At ~2 to 3.5 m NAVD88, the mud facies and brown sand facies deposits are sharply overlain by a bed of grey sand facies, except in six cores around the landward perimeter of the marsh, in which deposits of grey sand facies are absent at the depths sampled (Fig. 2). The contact between deposits of mud facies and the overlying grey sand facies, hereafter referred to simply as “the contact” (Fig. 3), is directly sampled in 7 cores and represents a distinct lithostratigraphic, geochemical, and biological boundary. It is interpreted to represent an abrupt environmental change from a marsh environment (as indicated by mud facies deposits) to a relatively lower elevation estuarine/lagoonal environmental (as indicated by grey sand facies deposits). The contact itself is sharp (<1 mm) or irregular, indicating nondeposition or erosion. The grey sand facies deposits above the contact often contain muddy rip up clasts, indicating the contact represents a high energy, erosive event.

While both the XRF and $\delta^{13}C$ data are highly variable, their general patterns are consistent with interpretations of an abrupt environmental change at the contact that emplaced relatively lower elevation grey sand facies deposits on higher elevation mud facies deposits. The mud below the contact has low Sr/Ti and Ca/Ti and high Fe/Ti ratios, but this pattern abruptly reverses above the contact. Sr and Ca ratios have been qualitatively associated with increased salinity (Koutsodendris et al., 2017), although they can also indicate the presence of freshwater carbonate (Chague-Goff et al., 2017). Therefore, we suggest the increase in Sr and Ca above the contact may indicate an increase in marine influence, relative to the sediments below the contact, but additional research (calibrations or identification of marine diatoms, for example) would be needed to confirm this interpretation. In addition, the bulk sediment $\delta^{13}C$ values gradually increase above the contact, potentially reflecting an increase in marine carbon input, as has been interpreted in other studies (Milker et al., 2015). The gradual nature of this change and variability of $\delta^{13}C$ values within grey sand facies deposits likely reflects the mixed sources of carbon present, which would include both marine derived carbon as well as redeposited carbon from estuarine sources (as rip ups, etc.).

Above the contact, the nature of the grey sand facies is highly variable and individual beds of sand are difficult to correlate spatially. Deposits of grey sand facies grade upwards into the top-most sediments in the marsh—beds of mud facies interbedded with beds of brown sand facies (Fig. 3) (Reynolds et al., 2018). We interpret this transition to represent the gradual shoaling of the estuary to its previous elevations and the marsh/mudflat environment that characterizes the marsh today.

The core stratigraphy suggests the contact is correlative throughout the marsh where grey sand facies deposits are found. In addition, a geotechnical survey from 2004 (Fugro West, 2004)

includes Cone Penetration Test (CPT) and borehole data from the eastern side of the marsh, which was interpreted to reflect grain size changes in the subsurface. The general grain size patterns indicate a contact between finer grained deposits and overlying sand deposits (described as grey or brown estuarine sand where sampled) at similar elevations to those of the contact we observe in our cores in other regions of the marsh, indicating that the contact may extend at least along the entire shore-parallel length of the marsh, and as far landward as Carpinteria Ave (Fig. 1).

Quantifying the magnitude of RSL change

The lithological and biological evidence presented above indicates that the contact marks a deepening of the estuary from a higher elevation (intertidal) mudflat/marsh environment characterized by fine grained sediment deposition of mud facies sediments to a lower elevation (subtidal to intertidal), tidally-influenced sand flat or shallow lagoon environment in which grey sand facies sediments were deposited. To estimate the magnitude of the inferred deepening, we estimated the indicative meaning, i.e., the vertical relationship to a reference water level (Shennan, 1986; van de Plassche, 1986), of the deposits above and below the contact, using the modern distribution of invertebrates as a guide (Fig. 4., Table 1).

In Carpinteria Marsh today, *C. californica* are found on the mudflats and high marsh surface (Bentz et al., 2016), which is consistent with previous studies that describe their elevation range as dominantly high intertidal (above MSL) in the southwest Pacific coast (MacDonald, 1969a; Macdonald, 1969b; Sousa, 1983). Therefore, we estimate that the mud facies deposits below the contact formed between the paleoelevations of Mean Low Water (MLW) and Highest Astronomical Tide (HAT), a range which is slightly more conservative than

that used for undifferentiated marsh deposits in other sea-level reconstructions from the Pacific coast of North America (Engelhart et al., 2015; Reynolds and Simms, 2015).

The bivalve species found above the contact within grey sand facies deposits occur at a wide range of elevations in estuaries and shallow coastal environments along the Pacific coast of North America (Fig. 4; Supplemental Materials 4) and their estuarine elevation ranges relative to tidal datums have not been systematically surveyed. However, the suite of species found in the grey sand facies are described as having “preferred’ or “common” ranges in lower intertidal to subtidal environments (see Supplemental Materials 4 and references therein); therefore, we estimate that the grey sand facies was deposited below Mean Sea Level (MSL). Due to the wide depth range of the species present (Fitch, 1953), it is also not possible to determine a definitive lower bound for the grey sand facies. However, the species present in the grey sand facies have been historically common in estuaries and shallow intertidal environments in southern California (Crooks, 2001; Desmond et al., 2002; Novoa et al., 2016) and paleoecological studies suggest that intertidal salt and mud flats were more common prehistorically than open lagoon conditions (Beller, 2014); therefore, we estimate that the grey sand facies was deposited between the elevations of the Lowest Astronomical Tide (LAT) and MSL, consistent with the indicative range used for undifferentiated lagoon/estuarine samples in the RSL reconstruction of Reynolds and Simms (2015). However, due to this uncertainty in elevation at which the grey sand facies was deposited, the calculated elevation change should be considered a minimum value.

The indicative ranges defined here are consistent with (1) other palaeoecological interpretations of the depth range of similar communities (i.e., Crooks et al., 2001); (2) indicative ranges defined in other Pacific coast sea level studies (i.e., Engelhart et al., 2015); and (3) the modern elevation distributions of these environments as surveyed in studies from other locations

along the Pacific coast of North America (see Supplemental Materials 4 and references therein). Marsh platforms in California marshes were found to dominantly occur at MHHW ± 0.5 m (the specific range depends on the tidal range of the individual marsh) (Thorne et al., 2018). In Carpinteria, the modern marsh platform (including Salicornia marsh and mudflats) is found between MLW and MHHW. In Mugu Lagoon, just to the south of Carpinteria, the marsh platform ranges from MSL to > MHHW. Older literature also supports these interpretations—MacDonald, 1969, who surveyed estuarine environments in California, found that marsh environments occurred between MLHW (mean lower high water) and EHW (extreme high water), which is approximately equivalent to MHW-HAT.

Following other studies (Hawkes et al., 2011; Hawkes et al., 2010; Pre et al., 2012; Woodroffe and Barlow, 2015), we use the modern elevations of relevant tidal datums (MLW and MSL from Carpinteria Marsh (Sadro et al., 2007); LAT and HAT from the Santa Barbara Station NOAA tide gauge (http://tidesandcurrets.noaa.gov, present tidal epoch data)) to calculate the magnitude of RSL change at the contact, as follows:

$$RSL\triangle = E_{pre} - E_{post} \quad (1)$$

where $RSL\triangle$ is magnitude of change in RSL, E_{pre} is the elevation, relative to MSL, of the below-contact marsh surface, and E_{post} is the elevation, relative to MSL, of the above-contact estuary surface.

The uncertainty in this calculation, $RSL\triangle_{error}$, is determined as follows:

$$RSL\triangle_{error} = \mathrm{sqrt}\left(E_{pre,error}^{\ 2} + E_{post,error}^{\ 2} \right) \quad (2)$$

where $E_{pre,error}$ is the indicative range of the mud facies deposits below the contact and $E_{post,error}$ is the indicative range of the grey sand facies deposits above the contact. Following other studies

(i.e.,(Hijma et al., 2015; Khan et al., 2019)), this uncertainty is assumed to approximate a 2σ vertical error.

Using these calculations, the contact represents a 1.3 ± 1.1 m rise in RSL; the characteristics described above suggest this rise in RSL caused a marsh/mudflat environment to transform to lower elevation intertidal sand flats. Because no abrupt rises in RSL have been inferred in late Holocene sea-level reconstructions for California (Reeder-Myers et al., 2015; Reynolds and Simms, 2015; Yousefi et al., 2018), we interpret this rise in RSL to represent subsidence of the marsh surface. In addition, the irregular/sharp nature of the contact and presence of muddy rip up clasts in the grey sand facies deposits above the contact indicate that the contact-forming event was erosive, abrupt and followed by high energy deposition.

Chronology of the Contact

To place Carpinteria Marsh's sea level history in a regional context, we used each radiocarbon age from Carpinteria Marsh as a sea-level index point (Shennan, 1986; van de Plassche, 1986) with an indicative range indicated by the facies it is associated with. We calculated the paleo RSL represented at each radiocarbon sample following the methods described in Reynolds and Simms, 2015 (Fig. 5). Unlike in Reynolds and Simms, 2015, we did not apply a tectonic correction (in order to illustrate any tectonic effects on the marsh). Therefore, the vertical error includes uncertainty in the ground surface elevation and the indicative range; compaction was neglected. Radiocarbon ages show that sedimentation in Carpinteria Marsh was ~0.2 cm/yr from ~7 to 3 ka, consistent with regional rates of sea-level rise at that time (Yousefi et al., 2018), although all ages from mud facies deposits are at lower elevations than would be expected from the regional sea-level record (Fig. 5).

After ~3.0 ka the sedimentary history among cores becomes more variable. Radiocarbon ages from samples in mud facies deposits just below the contact range from 1 to 3 ka over a limited vertical range (within 25 cm below the contact), indicating erosion, non-deposition, or compaction of sediments from this time period. Ages from samples above the contact, from the grey sand facies deposits, are variable and often out of stratigraphic order within their core, indicating reworking, or have overlapping age ranges, indicating rapid sedimentation. This variability in radiocarbon ages introduces significant uncertainty in the timing of the contact formation. Therefore, to test whether the contact formed synchronously and determine its age, we used two different methods, each with their own limitations and assumptions. Prior to running the age models, we removed seven ages that had two conditions indicative of reworking/contamination: (1) they were out of stratigraphic order within their core; and (2) the sample dated had other indications of reworking (small sample size, multiple fragments, evidence for bioturbation, etc.) or modern contamination (was described as a root) (Table 2).

First, we used the Bayesian age-depth model, Bacon (Blaauw and Christen, 2011) and calculated the age of the contact separately in each of the six cores that continuously sampled across the contact and had ages both above and below it (Supplemental Materials 3). Because an erosional contact represents missing time, the age-depth model was set to assume a hiatus of unknown duration at the contact. Because of the lithological change at the contact, we assumed the sedimentation rates above and below the contact were independent. For all age-depth models, a gamma distribution representing a mean accumulation rate of 0.4 cm/yr was used as the prior value for the sediments above the contact. This value is the average sedimentation rate previously calculated from Pb^{210}, Cs^{137}, and pollen/pollution horizons (Reynolds et al., 2018) for the upper 1-2 m of sediment in Carpinteria Marsh. The prior value used for the accumulation rate

of sediments below the contact was 0.2 cm/yr, which is the sedimentation rate we calculated from a linear regression between all calibrated ages and depths below NAVD88 values below the contact ([depth relative to NAVD88 (cm)] = 0.2 cm/yr * [cal yr BP] + 149 cm, $R^2 = 0.93$). The stratigraphy above and below the contact (the presence of beds of brown sand facies and spatial variability in the thickness of the grey sand facies deposits) indicates that sedimentation is temporally variable; however, the average sedimentation rates used for the priors result in age-depth models that fit the observed ages reasonably well (see Supplemental Materials 3).

Using separate chronologies for each core (no synchronicity is assumed between cores), the contact dates to (mean and 2σ range, cal years BP): 0.9 ± 0.2 ka (CM15), 1.2 ± 0.2 ka (CM20), 1.2 ± 0.2 ka (CM19), 0.9 ± 0.2 ka (CM21), 1.1 ± 0.1 ka (CM41) and 1.1 ± 0.1 ka (CM44). Each age-depth model relies on a very limited number of ages; therefore, any reworked ages or erosion may bias the age models, contributing to variability between cores. Regardless, the ranges of the modeled ages of the contact overlap, suggesting the contact formed synchronously across the marsh between 0.7 and 1.4 ka.

Because the Bacon age-depth models use assumptions about sedimentation rates and require us to identify the contact as a hiatus in order for the model to recognize it as such, we also calculated the age of the contact using the Bayesian age-depth model OxCal v4.4.4 (Lienkaemper and Ramsey, 2009; Ramsey, 2009), which (when using the Sequence and Phase functions) requires assumptions about stratigraphic order but not sedimentation rates. In this model, we used 47 radiocarbon ages from seven cores that continuously sampled across the contact, because their vertical distance from the contact could be established. Following Lienkaemper and Ramsey, 2009, we grouped data from multiple cores into a single stratigraphic package (same facies and similar depth relative to contact), termed a “Phase” in the program.

The ages within each phase were not constrained to a particular order in the model (although they are shown in chronological order for clarity in Fig. 6), but the phases themselves are constrained to be sequential—i.e., the stratigraphically lower phases are assumed to have occurred before those stratigraphically above them. Based on this model, the contact formed 1173-1231 cal years BP (2σ age range), which overlaps the contact age modeled using Bacon. However, any inherited ages in the GSF phase above the contact could bias this model old; therefore, we consider this modeled age to be a maximum. Taken together, the Bacon and OxCal models suggest the contact formed between 0.7 and 1.3 ka, hereafter given as 1.0 ± 0.3 ka (represent the midpoint and range of possible ages). The plethora of ages above the contact between 0.5 and 1 ka qualitatively supports this interpretation—it suggests that sediment started rapidly accumulating sometime after 1 ka.

The landward limit of deposition of grey sand facies (and therefore long-lasting post-seismic flooding) is indicated by the lack of grey sand facies deposits in several cores around the landward margins of the marsh (Fig. 2). The deepest of these cores, CM16, extends to 4 m depth below ground surface (1.6 m relative to NAVD88 at this core). This core contains a bed of brown sand facies with convolute bedding, possibly produced by earthquake-induced liquification, which dates to 0.9 ± 0.1 ka (2σ uncertainty, based on a separate Bacon age-depth model) and overlaps the time of formation of the contact. The lack of marine-influenced sand above this layer suggests that CM16 subsided from a higher pre-subsidence elevation and remained above MSL after subsidence or was subjected to less erosion and compaction than sediments from more seaward parts of the marsh.

DISCUSSION

Interpretation of the Contact

The evidence presented above suggests that the contact formed synchronously across the marsh at ~1.0 ± 0.3 ka due to an abrupt deepening of a marsh/mudflat environment that initiated rapid and high energy deposition of grey sand facies deposits in an intertidal to subtidal setting. The data presented are consistent with many of the criteria described elsewhere (Nelson et al., 1996; Nelson et al., 1998; Shennan et al., 2016) as indicative of coseismic subsidence: a laterally extensive and sharp contact; evidence for an RSL rise; and evidence for synchronicity of change, replicated in multiple cores. In addition, the paleo RSL values calculated for Carpinteria marsh consistently fall below what would be expected based on the paleo RSL calculated for other sites in southern California from 3 to 7 ka. If we raise the sea level index points below the contact by the maximum inferred subsidence amount (Fig. 5b), the modified paleo RSL ranges (while highly uncertain) overlap the lower part of the range in RSL values inferred for southern California (Reynolds and Simms, 2015; Yousefi et al., 2018). However, the Carpinteria values are still generally lower than those from other estuaries in southern California, perhaps indicating additional subsidence from compaction.

Carpinteria Marsh is located on the downthrown side of the RCF (Jackson and Yeats, 1982), a fault that offsets Quaternary gravels on shore (Dibblee Jr, 1994; Fredrickson, 2016; Jackson and Yeats, 1982). Therefore, movement on this fault is likely the source of subsidence observed and we argue that, while not a unique solution, coseismic subsidence is the most consistent explanation for the available data. However, nonseismic processes, such as floods, mouth or tidal channel migration, climate change-related sedimentation changes, or barrier breaching events can form stratigraphic changes similar to those created by coseismic subsidence (Nelson et al., 1998; Nelson et al., 1996). In the section below, we argue that the evidence is inconsistent with these alternative scenarios.

The ages of several large flood events recorded in the Santa Barbara Channel sedimentary record (Hendy et al., 2013) overlap the age of deposition of the upper bed of grey sand facies in Carpinteria Marsh. However, the grey sand facies deposits above the contact are bioturbated and contain radiocarbon dates that span 500 years of deposition, indicating this deposit represents a period of long-lasting environmental change, not a single event. Additionally, if the deposits of grey sand facies represented storm driven deposition, the repetition of flood layers in the Santa Barbara Basin (Du et al., 2018) would suggest multiple beds of grey sand facies should be present in the deeper cores, which we do not observe.

Tidal channel, mouth migration, or a transgressing shoreline could form a contact similar to that described here; however, these processes would be expected to cause progressive erosion through the marsh. For example, a transgressing shoreline would be expected to be more erosive ocean ward and less erosive landward, therefore being underlain by ages that young landward. In Carpinteria Marsh, the variable ages that underlie the contact exhibit no clear pattern relative to geography. The depth of the contact varies spatially (from -1.9 to -3.3 m relative to present MSL), deepening in the direction of area of greatest offset on the RCF (Jackson and Yeats, 1982), which may reflect a combination of differential subsidence, irregularity of the original marsh surface and spatial variability in erosion and/or compaction related to the subsidence event.

One possible explanation for the observed lack of radiocarbon ages between 1 and 3 ka would be a decrease in sedimentation during this time due to climatic changes that resulted in non-accumulation and/or erosion of the marsh for ~2000 years, before abruptly resuming sedimentation at 1.0 ka. However, at least four small streams pre-historically drained into Carpinteria marsh; therefore, a hiatus in sediment deposition by these streams would require all

entering streams to avulse away from the marsh at once, which would be unlikely. If a large-scale shift in climate were responsible, we would expect to see similar, contemporaneous responses from other estuaries in southern California—which does not appear to be the case from existing paleoecological records (Cole and Wahl, 2000; Ejarque et al., 2015; Lohmar et al., 1980). Instead, the erosion/nondeposition indicated from 1-3 ka likely reflects a combination of decreased sediment accumulation due to sea-level deceleration (Reynolds and Simms, 2015; Yousefi et al., 2018), as well as erosion and compaction induced by the subsidence event itself. Compaction/consolidation of surficial sediments has been documented in many historical subsidence events (Plafker, 1969; Weischet, 1963).

Finally, the contact could be attributed to abrupt breaching of a sandy barrier, which previously sheltered the estuary from marine influence (Nelson, 1992). Any scenario that does not call on tectonic subsidence, such as barrier breaching and all other alternatives mentioned previously, would require that the mud facies deposits below the contact were deposited ~1-3 m below MSL from 7 to 3 ka (see discrepancy between ages from Carpinteria marsh sediment and the regional RSL curve in Fig. 5). However, the geochemical characteristics of the mud facies deposits and the presence of *C. californica* suggest that the mud facies sediments were deposited in an intertidal environment, above MLW. Additionally, the environmental change represented by the contact appears to be laterally continuous and synchronous across much of the modern marsh, and possibly beyond its present boundaries, which would be difficult to accomplish in a single barrier breach. Therefore, we argue that coseismic subsidence is the most consistent explanation for the available data.

Hazard Implications

If a subsidence event were to recur today along the highly populated Santa Barbara coast, effects would include coastal flooding, ecological community shifts, damage to infrastructure due to liquefaction, and increased susceptibility of low-lying coastal areas to storms and sea-level rise (Hughes et al., 2015; Imakiire and Koarai, 2012; Jaramillo et al., 2017). However, the linear sedimentation rate from 3-7 ka and absence of stratigraphic evidence for older subsidence events suggests that the recurrence interval for large coseismic subsidence in Carpinteria may be greater than 6 kyrs, or that previous coseismic events did not result in an environmental change large enough to be identified in the stratigraphy.

The most likely source of subsidence within Carpinteria Marsh is movement along the RCF as a backthrust event off a larger fault in the region (Levy et al., 2019). The age range for the Carpinteria subsidence event overlaps that of the most recent large earthquake at Pitas Point near Ventura, dated to approximately $0.95^{+0.14/-0.11}$ ka (Rockwell et al., 2016). Assuming these two events are correlated would support the potential for large-scale ruptures within the Ventura/Santa Barbara regions. However, no other stratigraphic changes clearly indicative of uplift or subsidence are present in the Carpinteria record, while three other uplift events that occurred during the last 7000 years have been documented at Pitas Point. This discrepancy may suggest that movement along the larger thrust faults in the region only occasionally activates the RCF or that previous subsidence events were too small to be recognized in the stratigraphy.

Sedimentary Response of Structural Estuaries to Subsidence

The Carpinteria estuary responded to the coseismic increase in accommodation with a rapid accumulation of intertidal sediments (grey sand facies), similar to the responses of estuaries observed after historical coseismic events (Atwater et al., 2001; Ovenshine et al., 1976; Weischet, 1963) and well-dated prehistorical events in the stratigraphic record (Atwater and

Hemphill-Haley, 1997; Benson et al., 2001). The characteristics of the grey sand facies sediments suggest they were deposited in a high-energy tidal sand flat environment formed over the prior marsh and mudflat deposits (mud facies). The presence of marine species and silt-sand couplets in the grey sand facies deposits reflects an increased tidal influence after subsidence, perhaps representing a temporary increase in the tidal range as the estuary deepened and became more open to the ocean. However, as indicated by the lack of grey sand facies deposits in CM16 and the variability in the depth of the contact, the effects of coseisimc subsidence varied throughout the marsh perhaps due to variations in the pre-subsidence elevation as well as post-subsidence erosion and compaction.

Although the radiocarbon data suggests a rapid accumulation of intertidal sediments immediately following the subsidence event, the gradual shoaling of the estuary to its pre-subsidence elevation ultimately lasted 500-900 years, consistent with observations (Atwater et al., 2001; Benson et al., 2001; Reinhardt et al., 2010) that estuaries with smaller tidal ranges take longer to recover (in terms of their elevations) from coseismic subsidence, relative to those with larger tidal ranges, and therefore would not as readily preserve evidence of temporally-close events. This lag was likely exacerbated in Carpinteria by the Mediterranean climate and lack of large river influences, which limited the input of fluvial sediments, in contrast to the rapid accumulation of deltaic and fluvial deposits observed following subsidence events in estuaries and wetlands fed by permanent streams (Clark et al., 2013; Cochran et al., 2017; Knudsen et al., 2002; Reinhardt et al., 2010).

The displacement of the paleomarsh surface deposits relative to their expected elevations based on regional RSL (Reynolds and Simms, 2015) (Fig. 5) is consistent with the results of other studies (Castro et al., 2010; Chelli et al., 2017; Clement and Fuller, 2018; Hayward et al.,

2010; Rodriguez-Ramirez et al., 2014; Simms et al., 2016; Tanabe et al., 2013) that indicate that structural estuaries contain thicker deposits of intertidal and alluvial sediments than would be expected from non-tectonic increases in accommodation alone. Coseismic subsidence also displaces older deposits downward, increasing their preservation potential. Previous research on the deep structure of the Carpinteria basin (Jackson and Yeats, 1982) suggests that it has been subsiding since the middle Quaternary. To accommodate the structure and depth of the basin, it is likely that the estuary has experienced many other coseismic events over its lifetime and preserves sediments from previous transgressions and highstands, as observed in other structural estuaries (Atwater et al., 1977).

CONCLUSIONS

Previous studies have argued that accommodation created by RSL rise is a prerequisite for stratigraphic preservation of coseismic events and that evidence for coseismic subsidence is not as well-preserved during times of RSL stagnation or fall (Dura et al., 2016; Kelsey et al., 2015). However, many of these studies focus on estuaries in subducting regions where elastic deformation (and/or interseismic uplift) decreases the permanent vertical change generated by subsidence. In contrast, deformation in Carpinteria, and in other structurally bound estuaries (Atwater et al., 1977; Simms et al., 2016), may result in non-elastic, permanent deformation. In Carpinteria, coseismic subsidence may have temporarily interrupted the typical maturation process described in classic estuarine facies models (Boyd, 2006; Dalrymple et al., 1992); it is possible that without late Holocene subsidence, Carpinteria Marsh may have transitioned from an estuary to a delta as RSL rise decelerated in the late Holocene. Future studies could test whether these implications are broadly applicable to other structurally-controlled estuaries, and whether structural estuaries contain stratigraphic evidence of environmental changes and

deformation events independent of the trajectory of the concurrent non-tectonic components of RSL.

This research indicates that abrupt, coseismic subsidence in fault-bounded estuaries in regions such as the Californian, Mediterranean, and other active coastlines, can be identified and quantified in the stratigraphic record using the same, well-established criteria as those used to differentiate subsidence from other estuarine processes along subduction and strike-slip margins. This study follows a long line of previous studies from active margins around the world that have demonstrated that accommodation created by tectonic subsidence, in addition to non-tectonic RSL rise, results in distinctive sedimentary and stratigraphic characteristics of active margin estuaries, such as high long-term rates of sedimentation, evidence for abrupt rises in RSL, and a recovery response dependent on sediment influx and tidal range. The identification of localized subsidence events in structural estuaries can help elucidate seismic hazards and may provide additional insights into subsurface relationships in complicated tectonic regions.

ACKNOWLEDGMENTS

This research was supported by the Southern California Earthquake Center (Contribution No. 7942; Grants No. 14008 and 15156), the Santa Barbara Coastal Long Term Ecological Research (LTER) project and the Japan Society for the Promotion of Science (JSPS KAKENHI, JP15KK0151 and JP17H01168). SCEC is funded by NSF Cooperative Agreement EAR-1033462 & USGS Cooperative Agreement G12AC20038. This material is based upon work supported by the National Science Foundation Graduate Research Fellowship under Grant No. DGE-1144085. We would like to thank our field and lab assistants, as well as Andrew Brooks, Chanda Bertrand, John Southon, David Griggs, Craig Nicholson, and Paul-Valentich

Scott. We'd also like to thank the several anonymous reviewers whose thoughtful and constructive comments have vastly improved this manuscript.

REFERENCES CITED

Addison, J. A., Finney, B. P., Jaeger, J. M., Stoner, J. S., Norris, R. D., and Hangsterfer, A., 2013, Integrating satellite observations and modern climate measurements with the recent sedimentary record: An example from Southeast Alaska: Journal of Geophysical Research-Oceans, v. 118, no. 7, p. 3444-3461.

Atwater, B. F., 1987, Evidence for great Holocene earthquakes along the outer coast of Washington State: Science, v. 236, no. 4804, p. 942-944.

Atwater, B. F., Hedel, C. W., and Helley, E. J., 1977, Late Quaternary depositional history, Holocene sea-level changes, and vertical crust movement, southern San Francisco Bay, California, US Govt. Print. Off.

Atwater, B. F., and Hemphill-Haley, E., 1997, Recurrence intervals for great earthquakes of the past 3,500 years at northeastern Willapa Bay, Washington: USGPO; Information Services [distributor], 2330-7102.

Atwater, B. F., Yamaguchi, D. K., Bondevik, S., Barnhardt, W. A., Amidon, L. J., Benson, B. E., Skjerdal, G., Shulene, J. A., and Nanayama, F., 2001, Rapid resetting of an estuarine recorder of the 1964 Alaska earthquake: Geological Society of America Bulletin, v. 113, no. 9, p. 1193-1204.

Avnaim-Katav, S., Gehrels, W. R., Brown, L. N., Fard, E., and MacDonald, G. M., 2017, Distributions of salt-marsh foraminifera along the coast of SW California, USA: Implications for sea-level reconstructions: Marine Micropaleontology, v. 131, p. 25-43.

Bakker, E., and Slack, G., 1984, An island called California: an ecological introduction to its natural communities, Univ of California Press.

Beller, E. B., S; Grossinger, RM; Longcore, T; Stein, ED; Dark, S; Dusterhoff, SD, 2014, Northern San Diego County Lagoons Historical Ecology Investigation: San Francisco Estuary Institute, v. 7222, p. 215.

Benson, B. E., Atwater, B. F., Yamaguchi, D. K., Amidon, L. J., Brown, S. L., and Lewis, R. C., 2001, Renewal of tidal forests in Washington State after a subduction earthquake in AD 1700: Quaternary Research, v. 56, no. 2, p. 139-147.

Bentz, M., 2016, Establishing Foraminifera Based Biofacies within Shallow Marine Deposits, Carpinteria Slough, CA. Implications for southern California Sea-Level Studies [M.S. Unpublished Master's Thesis]: University of California Santa Barbara.

Blaauw, M., and Christen, J. A., 2011, Flexible paleoclimate age-depth models using an autoregressive gamma process: Bayesian analysis, v. 6, no. 3, p. 457-474.

Bourgeois, J., and Johnson, S. Y., 2001, Geologic evidence of earthquakes at the Snohomish delta, Washington, in the past 1200 yr: Geological Society of America Bulletin, v. 113, no. 4, p. 482-494.

Boyd, R., 2006, Estuarine and incised-valley facies models: Facies models revisited, p. 171-235.

Castro, D. F., de Fátima Rossetti, D., and Pessenda, L. C. R., 2010, Facies, δ13C, δ15N and C/N analyses in a late Quaternary compound estuarine fill, northern Brazil and relation to sea level: Marine Geology, v. 274, no. 1-4, p. 135-150.

564 Chelli, A., Pappalardo, M., Bini, M., Bruckner, H., Neri, G., Neri, M., and Spada, G., 2017,
565 Assessing tectonic subsidence from estimates of Holocene relative sea-level change: An
566 example from the NW Mediterranean (Magra Plain, Italy): Holocene, v. 27, no. 12, p.
567 1988-1999.
568 Clark, K., Cochran, U., Berryman, K., Biasi, G., Langridge, R., Villamor, P., Bartholomew, T.,
569 Litchfield, N., Pantosti, D., and Marco, S., 2013, Deriving a long paleoseismic record
570 from a shallow-water Holocene basin next to the Alpine fault, New Zealand: GSA
571 Bulletin, v. 125, no. 5-6, p. 811-832.
572 Clement, A. J. H., and Fuller, I. C., 2018, Influence of system controls on the Late Quaternary
573 geomorphic evolution of a rapidly-infilled incised-valley system: The lower Manawatu
574 valley, North Island New Zealand: Geomorphology, v. 303, p. 13-29.
575 Cochran, U., Clark, K., Howarth, J., Biasi, G., Langridge, R., Villamor, P., Berryman, K., and
576 Vandergoes, M., 2017, A plate boundary earthquake record from a wetland adjacent to
577 the Alpine fault in New Zealand refines hazard estimates: Earth and Planetary Science
578 Letters, v. 464, p. 175-188.
579 Crooks, J. A., 2001, Assessing invader roles within changing ecosystems: historical and
580 experimental perspectives on an exotic mussel in an urbanized lagoon: Biological
581 Invasions, v. 3, no. 1, p. 23-36.
582 Cundy, A., Kortekaas, S., Dewez, T., Stewart, I., Collins, P., Croudace, I., Maroukian, H.,
583 Papanastassiou, D., Gaki-Papanastassiou, P., and Pavlopoulos, K., 2000, Coastal
584 wetlands as recorders of earthquake subsidence in the Aegean: a case study of the 1894
585 Gulf of Atalantiearthquakes, central Greece: Marine Geology, v. 170, no. 1, p. 3-26.
586 Dalrymple, R. W., Zaitlin, B. A., and Boyd, R., 1992, Estuarine facies models: conceptual basis
587 and stratigraphic implications: perspective: Journal of Sedimentary Research, v. 62, no. 6.
588 Darienzo, M. E., and Peterson, C. D., 1990, Episodic tectonic subsidence of late Holocene salt
589 marshes, northern Oregon central Cascadia margin: Tectonics, v. 9, no. 1, p. 1-22.
590 Desmond, J., Deutschman, D., and Zedler, J., 2002, Spatial and temporal variation in estuarine
591 fish and invertebrate assemblages: analysis of an 11-year data set: Estuaries, v. 25, no. 4,
592 p. 552-569.
593 Dibblee Jr, T. W., 1994, Geology of the Carpinteria-Rincon Creek Area Santa Barbara and
594 Ventura Counties, California.
595 Du, X., Hendy, I., and Schimmelmann, A., 2018, A 9000-year flood history for Southern
596 California: A revised stratigraphy of varved sediments in Santa Barbara Basin: Marine
597 Geology, v. 397, p. 29-42.
598 Dura, T., Engelhart, S. E., Vacchi, M., Horton, B. P., Kopp, R. E., Peltier, W. R., and Bradley,
599 S., 2016, The Role of Holocene Relative Sea-Level Change in Preserving Records of
600 Subduction Zone Earthquakes: Current Climate Change Reports, v. 2, no. 3, p. 86-100.
601 Engelhart, S. E., Vacchi, M., Horton, B. P., Nelson, A. R., and Kopp, R. E., 2015, A sea-level
602 database for the Pacific coast of central North America: Quaternary Science Reviews, v.
603 113, no. 0, p. 78-92.
604 Ferren, W. R., 1985, Carpinteria Salt Marsh: environment, history, and botanical resources of a
605 southern California estuary, Herbarium, Dept. of Biological Sciences, University of
606 California, Santa Barbara, v. 4.
607 Fitch, J. E., 1953, Common marine bivalves of California, California Department of Fish and
608 Game.

609 Fredrickson, S., 2016, The Geomorphic Transition between the Santa Barbara and Ventura Fold
610 Belts near Rincon Point, California: UC Santa Barbara.
611 Fugro West, I., 2004, Geotechnical report Carpinteria Salt Marsh enhancement confluence of
612 Franklin and Santa Monica Creeks Carpinteria California, *in* District, S. B. C. F. C., ed.:
613 Santa Maria, California.
614 Hawkes, A. D., Horton, B., Nelson, A., Vane, C., and Sawai, Y., 2011, Coastal subsidence in
615 Oregon, USA, during the giant Cascadia earthquake of AD 1700: Quaternary Science
616 Reviews, v. 30, no. 3-4, p. 364-376.
617 Hawkes, A. D., Horton, B. P., Nelson, A. R., and Hill, D. F., 2010, The application of intertidal
618 foraminifera to reconstruct coastal subsidence during the giant Cascadia earthquake of
619 AD 1700 in Oregon, USA: Quaternary International, v. 221, no. 1-2, p. 116-140.
620 Hayward, B. W., Wilson, K., Morley, M. S., Cochran, U., Grenfell, H. R., Sabaa, A. T., and
621 Daymond-King, R., 2010, Microfossil record of the Holocene evolution of coastal
622 wetlands in a tectonically active region of New Zealand: Holocene, v. 20, no. 3, p. 405-
623 421.
624 Heaton, T. J., Köhler, P., Butzin, M., Bard, E., Reimer, R. W., Austin, W. E., Ramsey, C. B.,
625 Grootes, P. M., Hughen, K. A., and Kromer, B., 2020, Marine20—the marine
626 radiocarbon age calibration curve (0–55,000 cal BP): Radiocarbon, v. 62, no. 4, p. 779-
627 820.
628 Hijma, M. P., Engelhart, S. E., Törnqvist, T. E., Horton, B. P., Hu, P., and Hill, D. F., 2015, A
629 protocol for a geological sea-level database: Handbook of Sea-Level Research, edited by:
630 Shennan, I., Long, AJ, and Horton, BP, Wiley Blackwell, p. 536-553.
631 Holmquist, J. R., Reynolds, L., Brown, L. N., Southon, J. R., Simms, A. R., and MacDonald, G.
632 M., 2015, Marine radiocarbon reservoir values in southern California estuaries:
633 interspecies, latitudinal, and interannual variability: Radiocarbon, v. 57, no. 3, p. 449-
634 458.
635 Hubbard, D. M., 1996, Tidal cycle distortion in Carpinteria salt marsh, California: Bulletin of the
636 Southern California Academy of Sciences, v. 95, no. 2, p. 88-98.
637 Hubbard, J., Shaw, J. H., Dolan, J., Pratt, T. L., McAuliffe, L., and Rockwell, T. K., 2014,
638 Structure and seismic hazard of the Ventura Avenue anticline and Ventura fault,
639 California: Prospect for large, multisegment ruptures in the western Transverse Ranges:
640 Bulletin of the Seismological Society of America.
641 Jackson, P. A., and Yeats, R. S., 1982, Structural evolution of Carpinteria Basin, Western
642 Transverse Ranges, California: Aapg Bulletin-American Association of Petroleum
643 Geologists, v. 66, no. 7, p. 805-829.
644 Johnson, S. Y., Hartwell, S. R., Sorlien, C. C., Dartnell, P., and Ritchie, A. C., 2017, Shelf
645 evolution along a transpressive transform margin, Santa Barbara Channel, California:
646 Geosphere.
647 Kelsey, H. M., Engelhart, S. E., Pilarczyk, J. E., Horton, B. P., Rubin, C. M., Daryono, M. R.,
648 Ismail, N., Hawkes, A. D., Bernhardt, C. E., and Cahill, N., 2015, Accommodation space,
649 relative sea level, and the archiving of paleo-earthquakes along subduction zones:
650 Geology, v. 43, no. 8, p. 675-678.
651 Khan, N. S., Horton, B. P., Engelhart, S., Rovere, A., Vacchi, M., Ashe, E. L., Törnqvist, T. E.,
652 Dutton, A., Hijma, M. P., and Shennan, I., 2019, Inception of a global atlas of sea levels
653 since the Last Glacial Maximum: Quaternary Science Reviews, v. 220, p. 359-371.

Knudsen, K. L., Witter, R. C., Garrison-Laney, C. E., Baldwin, J. N., and Carver, G. A., 2002, Past earthquake-induced rapid subsidence along the northern San Andreas fault: A paleoseismological method for investigating strike-slip faults: Bulletin of the seismological Society of America, v. 92, no. 7, p. 2612-2636.

Koutsodendris, A., Brauer, A., Reed, J. M., Plessen, B., Friedrich, O., Hennrich, B., Zacharias, I., and Pross, J., 2017, Climate variability in SE Europe since 1450 AD based on a varved sediment record from Etoliko Lagoon (Western Greece): Quaternary Science Reviews, v. 159, p. 63-76.

Levy, Y., Rockwell, T. K., Shaw, J., Plesch, A., Driscoll, N., and Perea, H., 2019, Structural modeling of the Western Transverse Ranges: An imbricated thrust ramp architecture: Lithosphere, v. 11, no. 6, p. 868-883.

Lienkaemper, J. J., and Ramsey, C. B., 2009, OxCal: Versatile tool for developing paleoearthquake chronologies—A primer: Seismological Research Letters, v. 80, no. 3, p. 431-434.

MacDonald, K., 1969a, Molluscan faunas of Pacific coast salt marshes and tidal creeks: The Veliger, v. 11, no. 4, p. 399-405.

Macdonald, K. B., 1969b, Quantitative studies of salt marsh mollusc faunas from the North American Pacific coast: Ecological Monographs, v. 39, no. 1, p. 33-60.

Marshall, S. T., Funning, G. J., Krueger, H. E., Owen, S. E., and Loveless, J. P., 2017, Mechanical models favor a ramp geometry for the Ventura-pitas point fault, California: Geophysical Research Letters, v. 44, no. 3, p. 1311-1319.

McNeill, L. C., Goldfinger, C., Yeats, R. S., and Kulm, L. D., 1999, The effects of upper plate deformation on records of prehistoric Cascadia subduction zone earthquakes: Geological Society, London, Special Publications, v. 146, no. 1, p. 321-342.

Milker, Y., Horton, B. P., Vane, C. H., Engelhart, S. E., Nelson, A. R., Witter, R. C., Khan, N. S., and Bridgeland, W. T., 2015, Annual and seasonal distribution of intertidal foraminifera and stable carbon isotope geochemistry, Bandon Marsh, Oregon, USA: Journal of Foraminiferal Research, v. 45, no. 2, p. 146-166.

Mitra, S., 2002, Fold-accommodation faults: AAPG bulletin, v. 86, no. 4, p. 671-693.

Nelson, A. R., Ota, Y., Umitsu, M., Kashima, K., and Matsushima, Y., 1998, Seismic or hydrodynamic control of rapid late-Holocene sea-level rises in southern coastal Oregon, USA?: The Holocene, v. 8, no. 3, p. 287-299.

Nelson, A. R., Shennan, I., and Long, A. J., 1996, Identifying coseismic subsidence in tidal-wetland stratigraphic sequences at the Cascadia subduction zone of western North America: Journal of Geophysical Research: Solid Earth, v. 101, no. B3, p. 6115-6135.

Novoa, A., Talley, T. S., Talley, D. M., Crooks, J. A., and Reyns, N. B., 2016, Spatial and temporal examination of bivalve communities in several estuaries of Southern California and Northern Baja California, MX: PloS one, v. 11, no. 2, p. e0148220.

Ovenshine, A., Lawson, D. E., and Bartsch-Winkler, S. R., 1976, The Placer River Silt—an intertidal deposit caused by the 1964 Alaska earthquake: J. Res. US Geol. Surv, v. 4, no. 2, p. 151-162.

Page, H. M., 1995, Variation in the natural abundance of N-15 in the halophyte, Salcornia-Virginica, associated with groundwater subsidies of nitrogen in a southern California salt marsh: Oecologia, v. 104, no. 2, p. 181-188.

Plafker, G., 1969, Tectonics of the March 27, 1964, Alaska earthquake.

Pratt, T. L., Troost, K. G., Odum, J. K., and Stephenson, W. J., 2015, Kinematics of shallow backthrusts in the Seattle fault zone, Washington State: Geosphere, v. 11, no. 6, p. 1948-1974.

Pre, C. A. G., Horton, B. P., Kelsey, H. M., Rubin, C. M., Hawkes, A. D., Daryono, M. R., Rosenberg, G., and Culver, S. J., 2012, Stratigraphic evidence for an early Holocene earthquake in Aceh, Indonesia: Quaternary Science Reviews, v. 54, p. 142-151.

Ramsey, C. B., 2009, Bayesian analysis of radiocarbon dates: Radiocarbon, v. 51, no. 1, p. 337-360.

Reeder-Myers, L., Erlandson, J. M., Muhs, D. R., and Rick, T. C., 2015, Sea level, paleogeography, and archeology on California's Northern Channel Islands: Quaternary Research, v. 83, no. 2, p. 263-272.

Reimer, P. J., Austin, W. E., Bard, E., Bayliss, A., Blackwell, P. G., Ramsey, C. B., Butzin, M., Cheng, H., Edwards, R. L., and Friedrich, M., 2020, The IntCal20 Northern Hemisphere radiocarbon age calibration curve (0–55 cal kBP): Radiocarbon, v. 62, no. 4, p. 725-757.

Reinhardt, E. G., Nairn, R. B., and Lopez, G., 2010, Recovery estimates for the Rio Cruces after the May 1960 Chilean earthquake: Marine Geology, v. 269, no. 1-2, p. 18-33.

Reynolds, L. C., and Simms, A. R., 2015, Late Quaternary relative sea level in southern California and Monterey Bay: Quaternary Science Reviews, v. 126, p. 57-66.

Rockwell, T. K., Clark, K., Gamble, L., Oskin, M. E., Haaker, E. C., and Kennedy, G. L., 2016, Large Transverse Range Earthquakes Cause Coastal Upheaval near Ventura, Southern California: Bulletin of the Seismological Society of America, v. 106, no. 6, p. 2706-2720.

Rodriguez-Ramirez, A., Flores-Hurtado, E., Contreras, C., Villarias-Robles, J. J. R., Jimenez-Moreno, G., Perez-Asensio, J. N., Lopez-Saez, J. A., Celestino-Perez, S., Cerrillo-Cuenca, E., and Leon, A., 2014, The role of neo-tectonics in the sedimentary infilling and geomorphological evolution of the Guadalquivir estuary (Gulf of Cadiz, SW Spain) during the Holocene: Geomorphology, v. 219, p. 126-140.

Sadro, S., Gastil-Buhl, M., and Melack, J., 2007, Characterizing patterns of plant distribution in a southern California salt marsh using remotely sensed topographic and hyperspectral data and local tidal fluctuations: Remote Sensing of Environment, v. 110, no. 2, p. 226-239.

Scott, D. B., Mudie, P. J., and Bradshaw, J. S., 2011, Coastal evolution of Southern California as interpreted from benthic foraminifera, ostracodes, and pollen: Journal of Foraminiferal Research, v. 41, no. 3, p. 285-307.

Shennan, I., 1986, Flandrian sea-level changes in the Fenland. II: Tendencies of sea-level movement, altitudinal changes, and local and regional factors: Journal of Quaternary Science, v. 1, no. 2, p. 155-179.

Shennan, I., Garrett, E., and Barlow, N., 2016, Detection limits of tidal-wetland sequences to identify variable rupture modes of megathrust earthquakes: Quaternary Science Reviews, v. 150, p. 1-30.

Sherrod, B. L., 2001, Evidence for earthquake-induced subsidence about 1100 yr ago in coastal marshes of southern Puget Sound, Washington: Geological Society of America Bulletin, v. 113, no. 10, p. 1299-1311.

Simms, A., Reynolds, L. C., Bentz, M., Roman, A., Rockwell, T., and Peters, R., 2016, Tectonic subsidence of California estuaries increases forecasts of relative sea-level rise: Estuaries and coasts, v. 39, no. 6, p. 1571-1581.

Sousa, W. P., 1983, Host life history and the effect of parasitic castration on growth: a field study of *Cerithidea californica* Haldeman (Gastropoda: Prosobranchia) and its trematode parasites: Journal of Experimental Marine Biology and Ecology, v. 73, no. 3, p. 273-296.

Survey, U. G., and Survey, C. G., 2006, Quaternary fault and fold database for the United States: US Geological Survey.

Tanabe, S., Nakanishi, T., Matsushima, H., and Hong, W., 2013, Sediment accumulation patterns in a tectonically subsiding incised valley: Insight from the Echigo Plain, central Japan: Marine Geology, v. 336, p. 33-43.

Thorne, K., MacDonald, G., Guntenspergen, G., Ambrose, R., Buffington, K., Dugger, B., Freeman, C., Janousek, C., Brown, L., and Rosencranz, J., 2018, US Pacific coastal wetland resilience and vulnerability to sea-level rise: Science Advances, v. 4, no. 2, p. eaao3270.

van de Plassche, O., 1986, Sea-level research: a manual for the collection and evaluation of data, Geo Books Norwich, England.

Weischet, W., 1963, Further observations of geologic and geomorphic changes resulting from the catastrophic earthquake of May 1960, in Chile: Bulletin of the Seismological Society of America, v. 53, no. 6, p. 1237-1257.

Weltje, G. J., and Tjallingii, R., 2008, Calibration of XRF core scanners for quantitative geochemical logging of sediment cores: theory and application: Earth and Planetary Science Letters, v. 274, no. 3, p. 423-438.

Wilson, R., Hemphill-Haley, E., Jaffe, B., Richmond, B., Peters, R., Graehl, N., Kelsey, H., Leeper, R., Watt, S., and McGann, M., 2014, The search for geologic evidence of distant-source tsunamis using new field data in California: Chapter C in The SAFRR (Science Application for Risk Reduction) Tsunami Scenario: US Geological Survey, 2331-1258.

Woodroffe, S. A., and Barlow, N. L., 2015, Reference water level and tidal datum: Handbook of Sea-Level Research, p. 171-180.

Yokoyama, Y., Koizumi, M., Matsuzaki, H., Miyairi, Y., and Ohkouchi, N., 2010, Developing ultra small-scale radiocarbon sample measurment at the University of Tokyo Radiocarbon, v. 52, no. 2, p. 310-318.

Yousefi, M., Milne, G. A., Love, R., and Tarasov, L., 2018, Glacial isostatic adjustment along the Pacific coast of central North America: Quaternary Science Reviews, v. 193, p. 288-311.

FIGURE CAPTIONS

Figure 1. Location of Carpinteria Marsh. Locations noted in manuscript, including major Quaternary faults (Survey and Survey, 2006). Carpinteria Marsh, the study site, is indicated by the white star. The location of the cross section is shown by the white line. The cross section in the bottom panel is adapted from Jackson and Yeats 1982 and Simms 2016.

Figure 2. Core Locations. Locations of vibracores and CPT boreholes (Fugro West, 2004) in Carpinteria marsh. The top panel shows Carpinteria in 1929; the bottom in 2007. Cores with grey sand facies are shown as black dots; cores that do not sample grey sand facies are shown as white dots. CPTs are shown as triangles. Cross sections illustrated in Figure 3 are shown as white lines. In both images, the alluvial fan attributed to a flood in 1914 (Ferren, 1985) is clearly visible in the marsh's northeast corner.

Figure 3. Marsh Stratigraphy and evidence for relative sea level change. Shore parallel core transect A, shore parallel CPT transect B (redrawn based on Fugro West, 2004, Plate 4a), and shore-perpendicular core transect C. Grey boxes indicate the depth of material sampled in sediment cores; dotted lines indicate the depth of borehole CPT data (Fugro West, 2004). The stratigraphy based on data from the Fugro West, 2004 report is based on their interpretations of grain size—sand deposits were re-interpreted here as correlative with GSF, while those described as clay/silt/fine grained were re-interpreted here as correlative with MF. BSF correlations are based on age and lithological data and are uncertain. Details of XRF and carbon isotope data are shown from Core 46. Radiocarbon ages are given in calibrated thousands of years BP; the ranges shown 2σ uncertainties. Several redundant radiocarbon ages from CM46 were removed from clarity; all ages are listed in Table 2 and are also shown in Supplemental Fig. S1.

Figure 4. Species depth ranges compiled from previously published materials through the Pacific coast of North America (detailed in Supplemental Materials 4). Black boxes indicate ranges quantitatively indicated and described as "preferred", "common" or "high density." Dashed lines indicate the possible range of the species, estimated from qualitative descriptions such as

805 “intertidal” or “lower intertidal.” The local tidal datums relative to NAVD88 are shown on the
806 left side of the figure; all these measurements are from Sadro et al., 2007 except the two starred
807 datums (LAT and HAT), for which Carpinteria-specific data was not available. LAT and HAT
808 were taken from the NOAA Santa Barbara tide gauge
809 (https://tidesandcurrents.noaa.gov/datums.html?id=9411340) datums from the present tidal
810 epoch. The indicative ranges of mud facies and grey sand facies, equivalent to the Eq 1. terms
811 Epre and Epost, respectively, are shown as estimated normal distributions with 2σ range
812 equivalent to the indicative range.
813
814 Figure 5. Chronology of the contact. (a) shows 2σ calibrated radiocarbon ages vs. paleo RSL
815 (calculated following Reynolds and Simms, 2015) relative to present MSL in all cores. The
816 vertical uncertainty is indicated by the height of the box and represents an approximately 2σ
817 uncertainty, which includes the indicative range of the sample and the uncertainty in the ground
818 surface elevation for each core, which was less than 0.15 m for all samples. The black lines show
819 the bounds of a Glacial Isostatic Adjustment (GIA) RSL model for southern California from
820 Yousefi et al., 2019, which was fit to paleo RSL data for other sites in southern California from
821 Reynolds and Simms, 2015 (shown as grey boxes). (b) shows the same data, but with the
822 Carpinteria ages beneath the contact raised by the maximum inferred subsidence of 2.36 m to test
823 whether the removal of coseismic displacement places Carpinteria’s paleo RSL within that
824 calculated for S. California.
825
826 Figure 6. OxCal v4.4.4 (Bronk Ramsey 2021) calibrated 2σ ages relative to contact and model of
827 contact age. Black distributions are posterior (calibrated) probability density functions and white

outlines are likelihood distributions based on given radiocarbon ages (Bronk Ramsey, 2009). Ages from a similar stratigraphic position relative to the contact and within the same facies were grouped into phases, as indicated by the black boxes (Lienkaemper and Bronk Ramsey, 2009). Terrestrial samples were calibrated in OxCal using IntCal20 (Reimer et al., 2020) and shell samples were calibrated in OxCal using Marine20 (Heaton et al., 2020), using estuarine marine reservoir values from (Holmquist et al., 2015) updated with the Marine20 Reservoir Database (http://calib.org/marine/). See Table 2 for radiocarbon sample details and reservoir values used for shell samples. The name of each R_Date indicates the type of material and its depth relative to the contact, i.e., PF811 = plant fragment from 811 cm below the contact. For ages below the contact (listed first in the script), the depth should be read as "cm below the contact", while for ages above the contact (listed further down in the script), the depth given should be read as "cm above the contact". PF = plant fragment; Sh = shell; Ch = charcoal; Wd = wood. Additional details about the radiocarbon ages and reservoir values are provided in Table 2 and in the main text.

[1]GSA Data Repository item 2021xxx, Supplemental Materials 1 (supplemental figures S1, S2, S3, S4); Supplemental Materials 2 (Table S1. Core Information); Supplemental Materials 3 (Bacon and OxCal Scripts); and Supplemental Materials 4 (Invertebrate depth references) is available online at www.geosociety.org/pubs/ft20XX.htm, or on request from editing@geosociety.org.

Figure 1. Site location and tectonic context

Figure 1

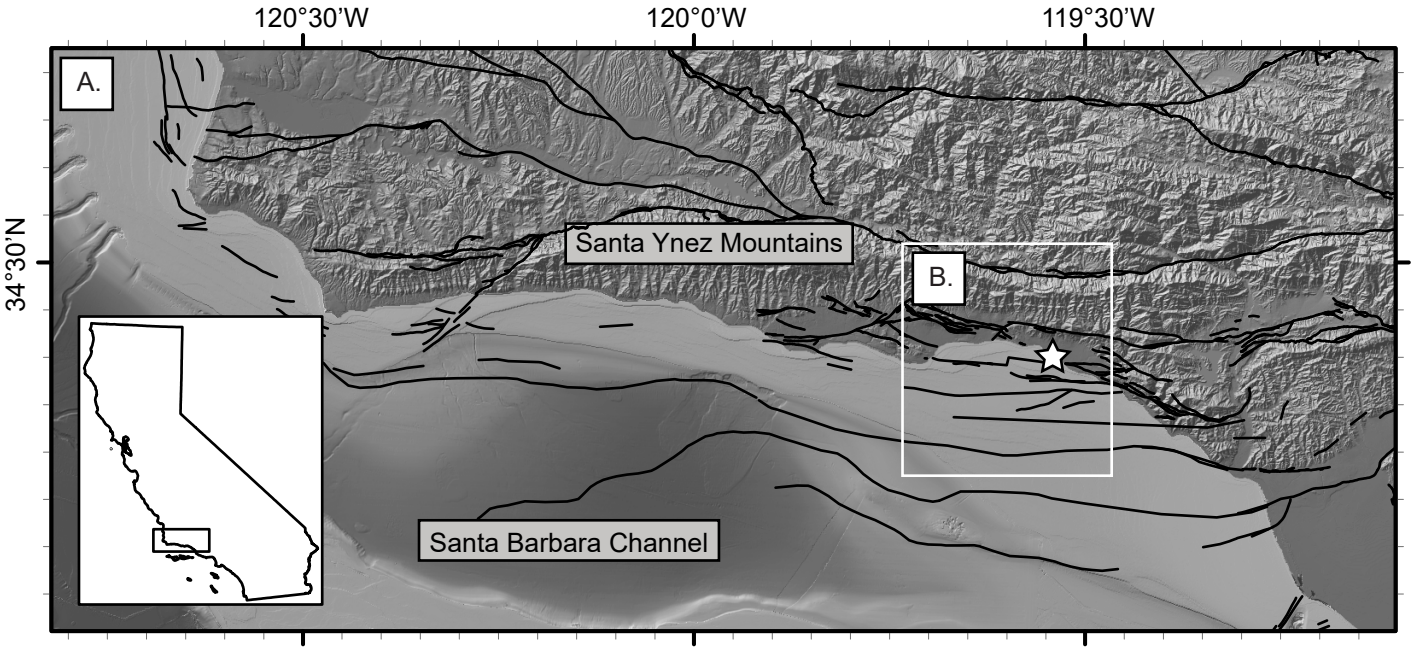

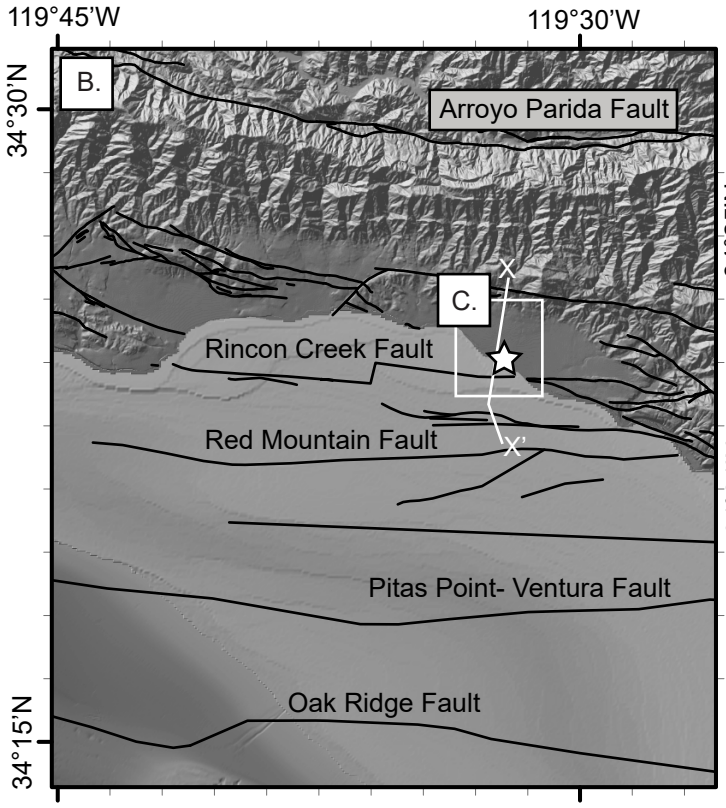

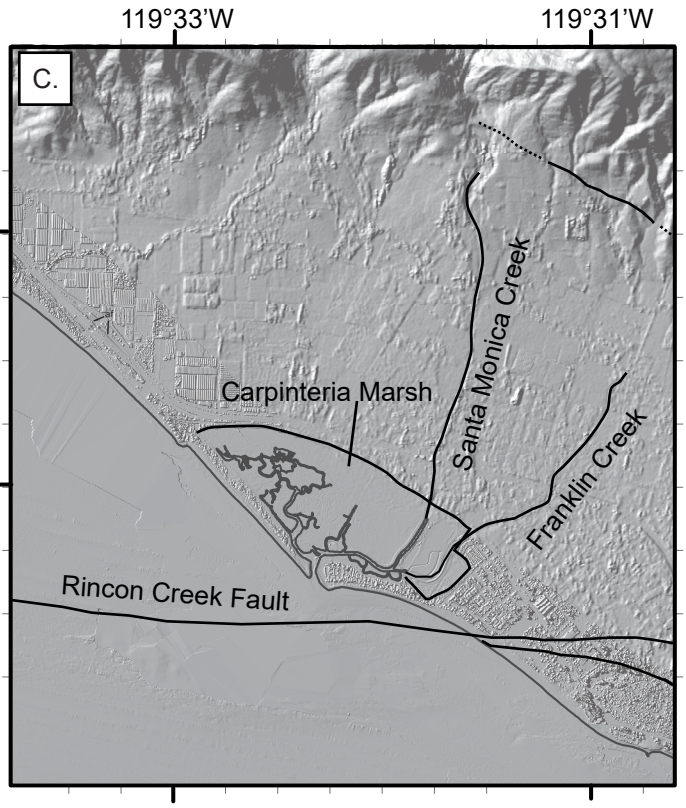

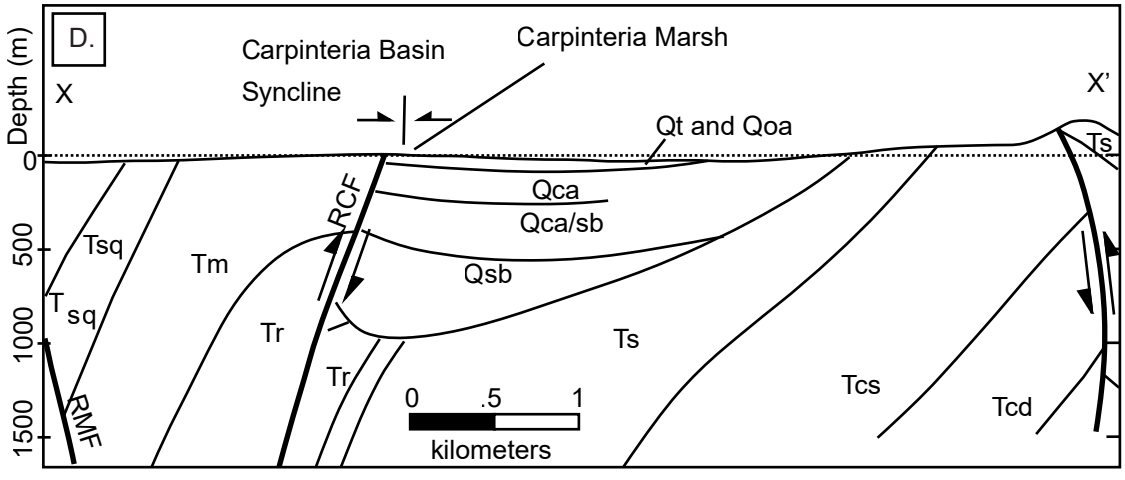

Figure 2. Core locations

Figure 2

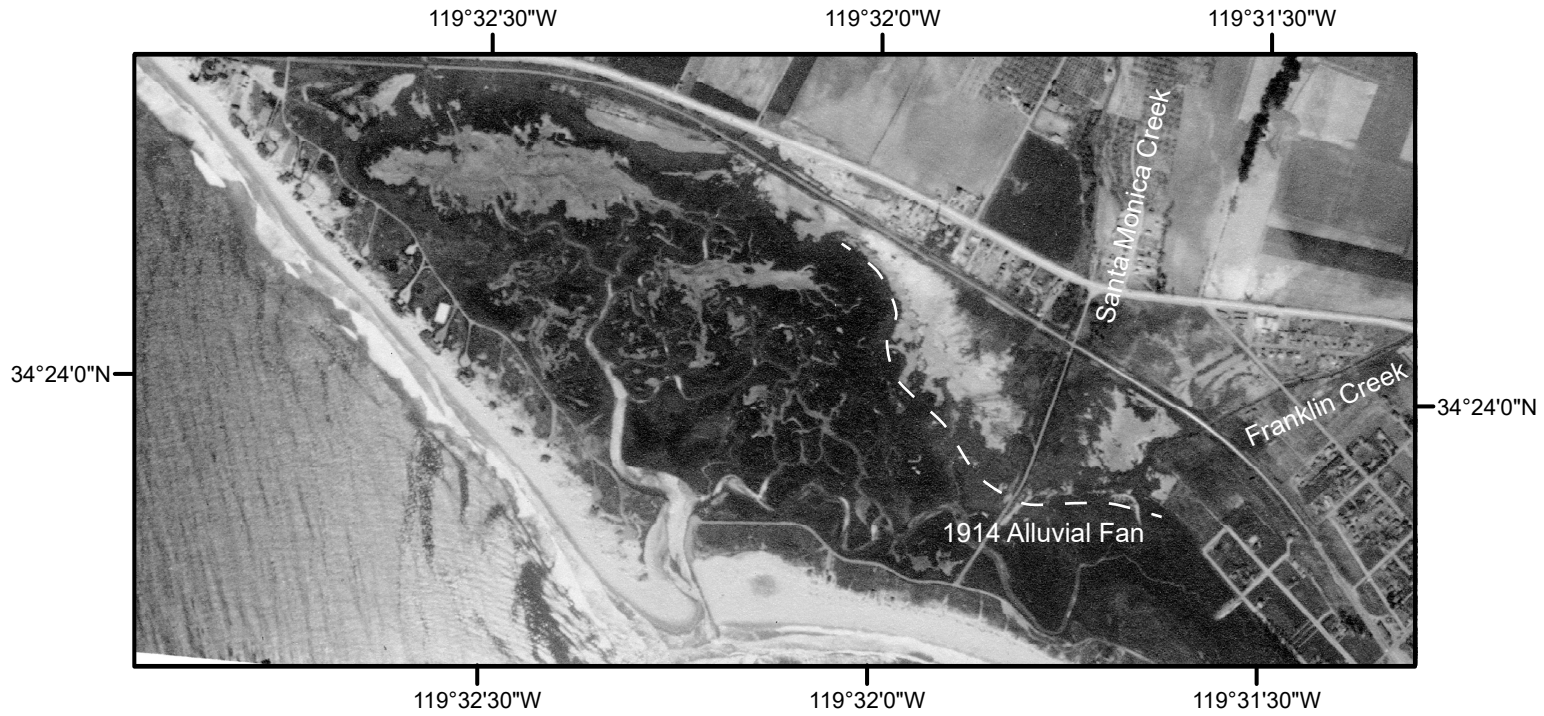

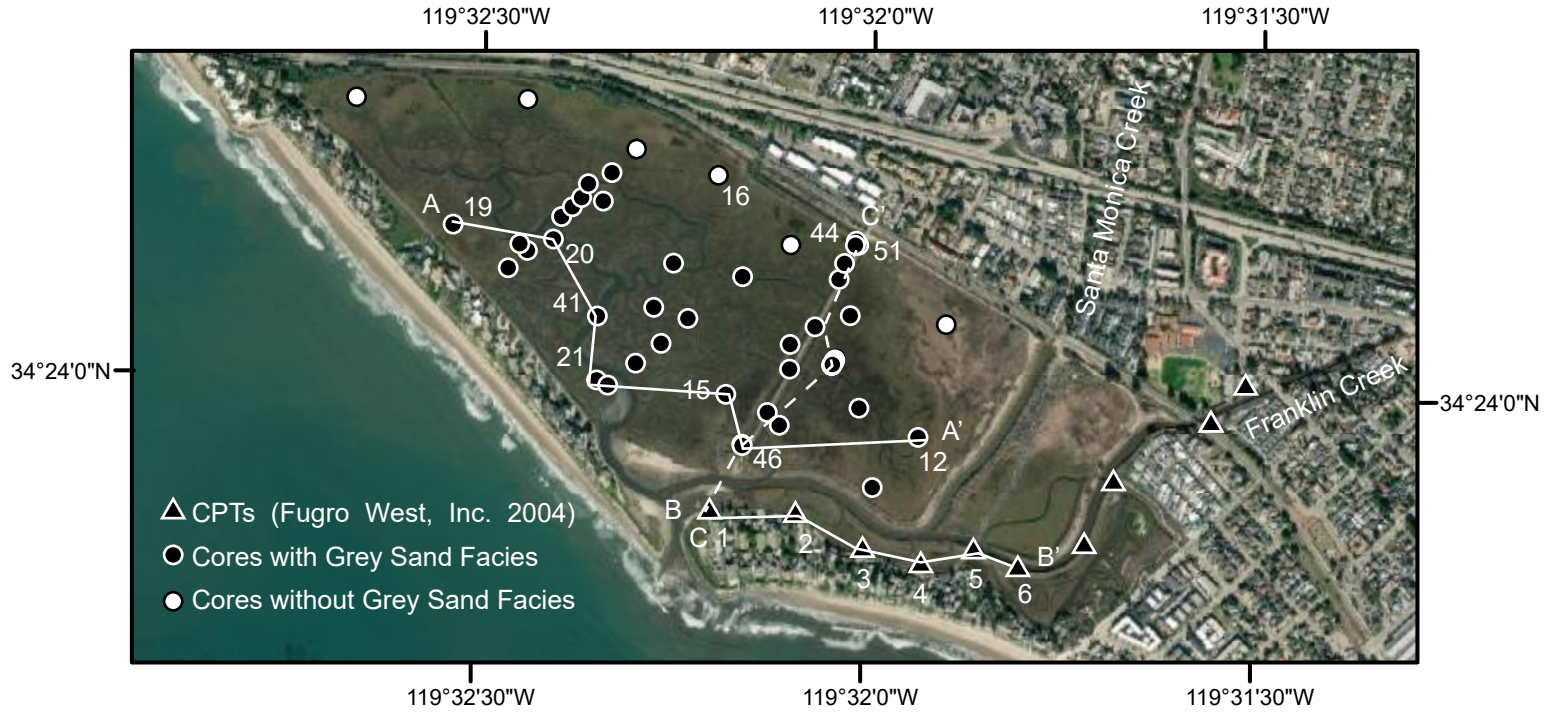

Figure 3. Marsh Stratigraphy and Evidence for RSL Change

Figure 3

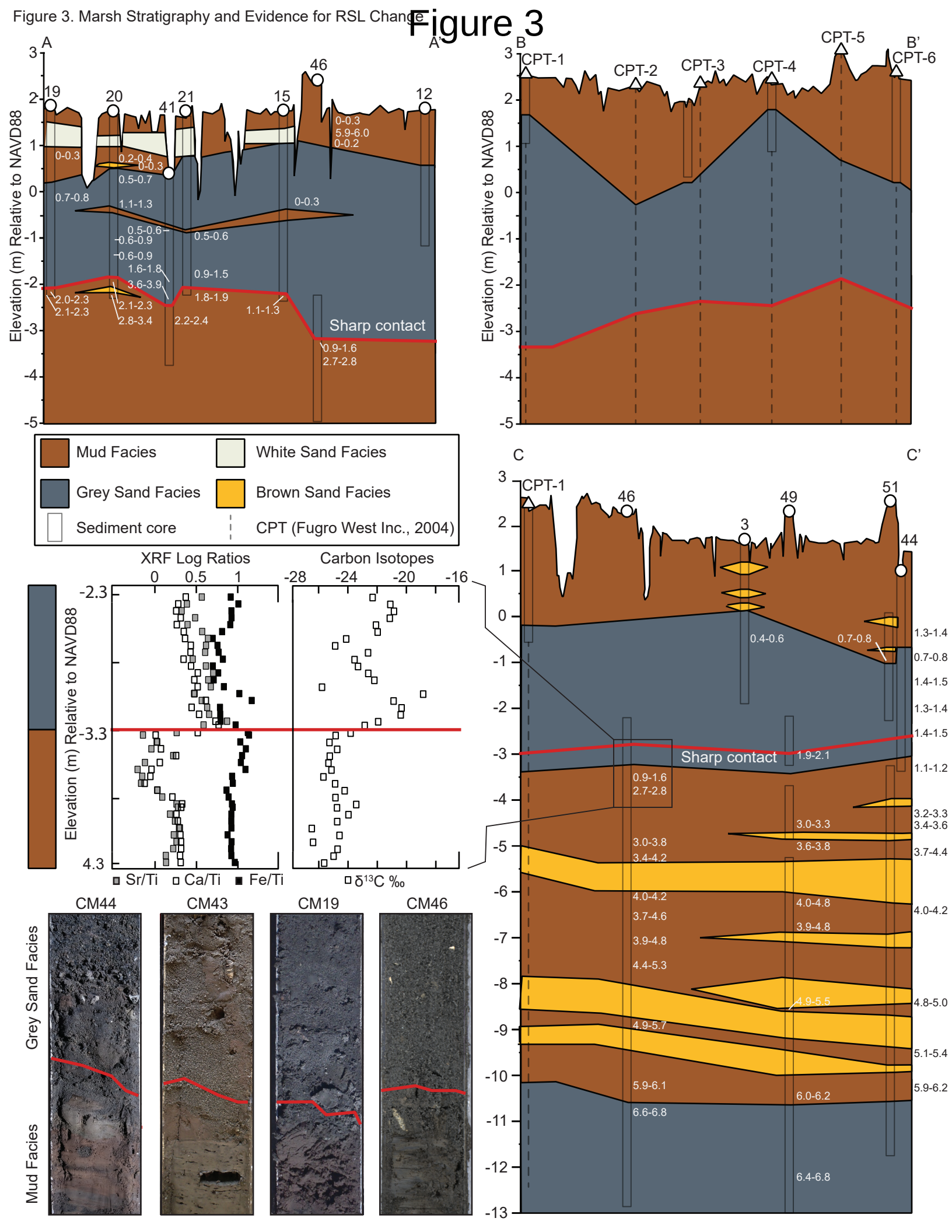

Figure 4. Species depth ranges.

Figure 4

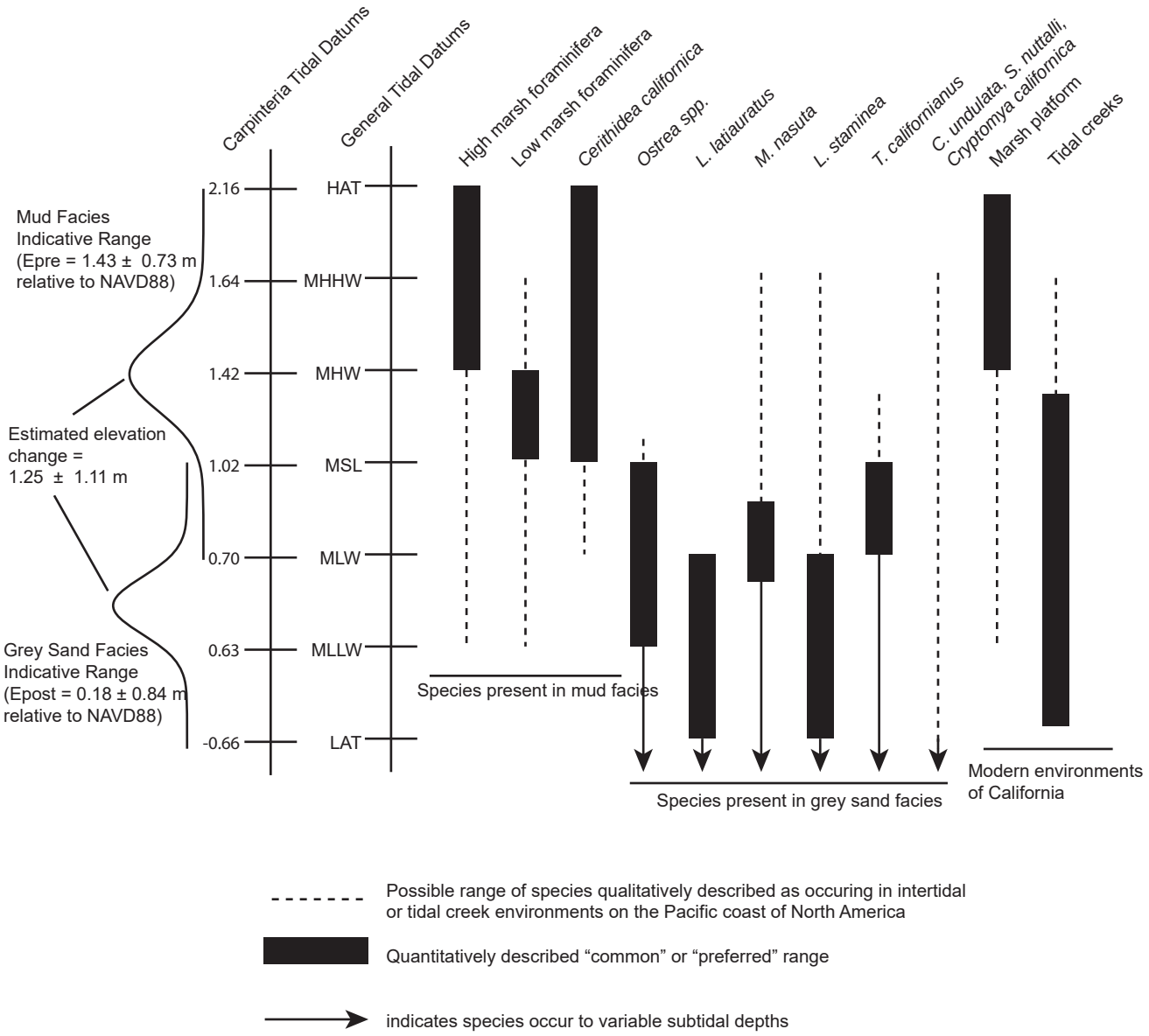

Figure 5

Figure 5. Paleo RSL Carpinteria Marsh vs. Southern California

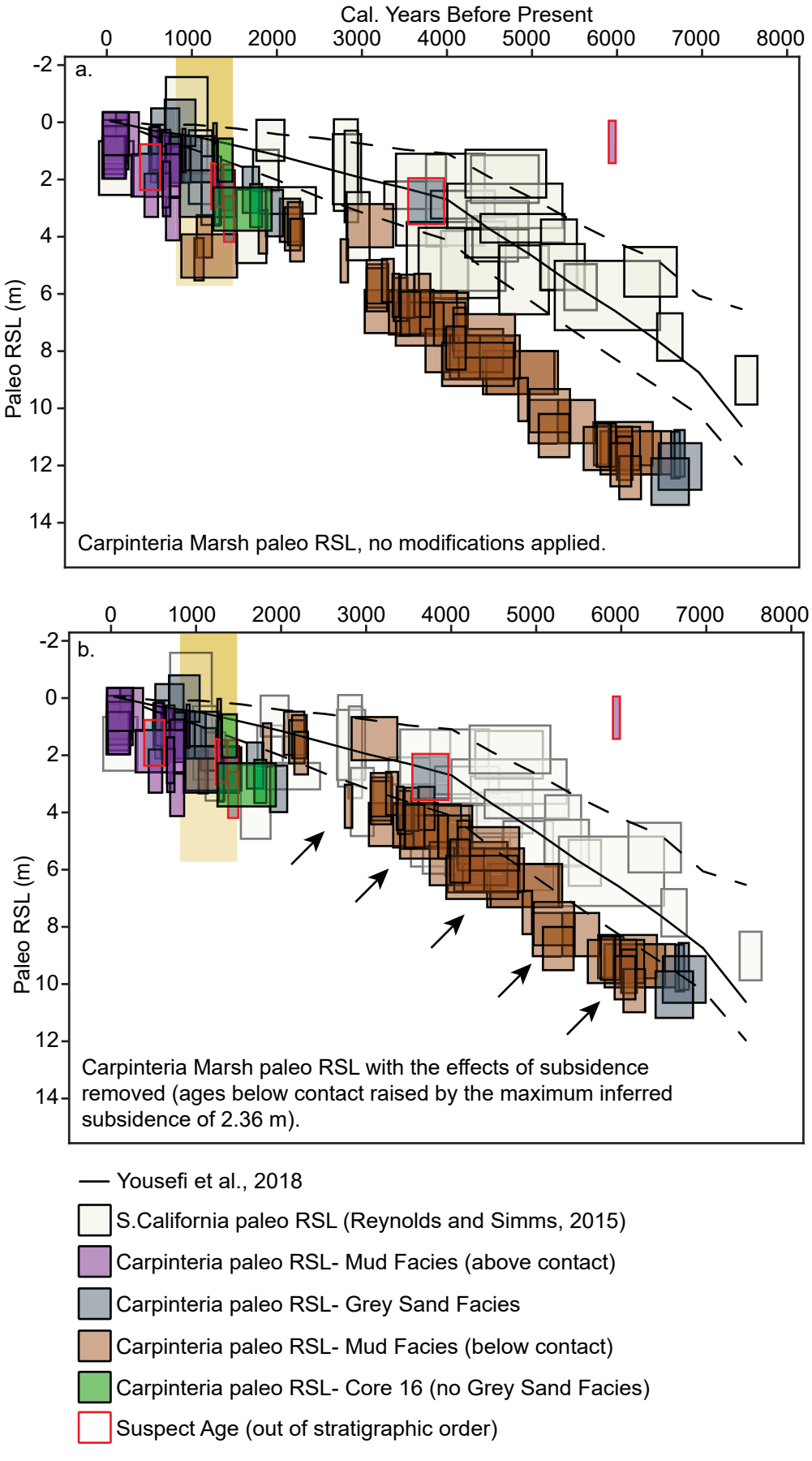

Figure 6

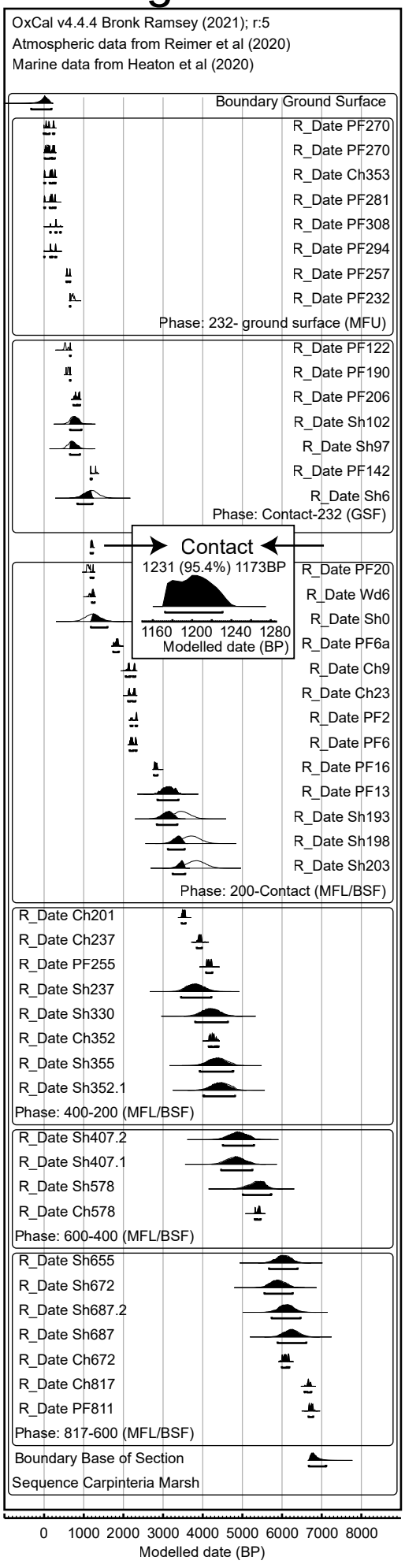
OxCal v4.4.4 Bronk Ramsey (2021); r:5
Atmospheric data from Reimer et al (2020)
Marine data from Heaton et al (2020)
Boundary Ground Surface
R_Date PF270
R_Date PF270
R_Date Ch353
R_Date PF281
R_Date PF308
R_Date PF294
R_Date PF257
R_Date PF232
Phase: 232- ground surface (MFU)
R_Date PF122
R_Date PF190
R_Date PF206
R_Date Sh102
R_Date Sh97
R_Date PF142
R_Date Sh6
Phase: Contact-232 (GSF)
Contact
1231 (95.4%) 1173BP
1160 1200 1240 1280
Modelled date (BP)
R_Date PF20
R_Date Wd6
R_Date Sh0
R_Date PF6a
R_Date Ch9
R_Date Ch23
R_Date PF2
R_Date PF6
R_Date PF16
R_Date PF13
R_Date Sh193
R_Date Sh198
R_Date Sh203
Phase: 200-Contact (MFL/BSF)
R_Date Ch201
R_Date Ch237
R_Date PF255
R_Date Sh237
R_Date Sh330
R_Date Ch352
R_Date Sh355
R_Date Sh352.1
Phase: 400-200 (MFL/BSF)
R_Date Sh407.2
R_Date Sh407.1
R_Date Sh578
R_Date Ch578
Phase: 600-400 (MFL/BSF)
R_Date Sh655
R_Date Sh672
R_Date Sh687.2
R_Date Sh687
R_Date Ch672
R_Date Ch817
R_Date PF811
Phase: 817-600 (MFL/BSF)
Boundary Base of Section
Sequence Carpinteria Marsh
0 1000 2000 3000 4000 5000 6000 7000 8000
Modelled date (BP)

Table 1. Facies Descriptions, interpretations, and indicative ranges.

Facies (Reynolds et al., 2018)	**Facies description**	**Facies Interpretation**	**Indicative Range**	**Indicative Range (modern values, relative to NAVD88)**
Mud Facies	organic-rich; fine-grained (clay to fine sand, mean grain size < 50 um); massive, mottled, or laminated; colors range from blue-grey to red-brown; whole and partial *Cerithidea californica* shells common, other shell fragments rare; sparse marsh and mudflat foraminifera, including *Jadammina macrescens*, *Milliammina fusca, Elphidium spp, Ammonia spp.*, and *Trochiammina* spp.; beds range from a few cm to 1 m thick; interbedded with brown sand facies	Marsh and mudflats	MLW* to HAT**	0.70 to 2.16 m
Grey Sand Facies	generally organic-poor, with some small (mm-scale) plant fragments; fine to medium sand (mean grain size 50-150 um); light to dark grey in color; poorly sorted, with few muddy silt lamina, frequently mottled or faintly laminated; abundant shells and shell fragments, including *Ostrea* spp., *Saxidomus nuttalli, Macoma nasuta, Leukoma laciniata*; devoid of foraminifera; beds m-scale in thickness; grade into or are sharply overlain by beds of mud facies or brown sand facies	Low intertidal or subtidal sand flats and/or lagoon	LAT** to MSL*	-0.66 to 1.02 m
Brown Sand Facies	organic-poor; sandy silt to medium sand (mean grain size 20-112 um); brown colored; poorly sorted, scattered granules, laminated, massive and normally graded beds; no shells or shell fragments or foraminifera; beds 1-50 cm thick; interbedded with mud facies and most common in the cores at the landward edges of the marsh	Alluvial fan (flood) deposits	> MLW*	> 0.70 m

**MLW, MSL modern values from Sadro et al., 2007*
***LAT, HAT modern values from NOAA (Santa Barbara Station NOAA tide gauge (http://tidesandcurrents.noaa.gov))*

Table 3. All radiocarbon data. Radiocarbon ages were calibrated using CALIB 8.2 (Stuiver et al., 2021), which uses the IntCal20 (Reimer et al., 2020) and Marine20 (Heaton et al., 2020) calibration curves. The delta R values used are 120 +/-78 for bivalve and oyster shells; 34 +/-160 for *Cerithidea* following Holmquist et al., and re-calculated using the Marine20 Reservoir Database (http://calib.org/marine/). Elevation error for core top elevations measured with lidar is assigned 0.15 m (average difference from differential GPS measurment from Sadro et al., 2015). Samples which were removed for analysis are noted in Notes column. Facies include Mud Facies (MF), Grey Sand Facies (GSF), and White Sand Facies (WSF), following Reynolds et al., 2018.

Lab	Lab No.	Material Description	Facies (following Reynolds et al., 2018)	Core Number	Sample Depth Below Ground Surface (cm)	14C age	14C error	lower cal range BP	upper cal range BP	median cal age BP	Paleo MSL rel to PMSL	Paleo MSL error	depth of sample relative to "contact"	Removed from Bacon Models?	Removed from OxCal model?	Other Notes
YAUT	26704	articulated bivalve (*Leukoma staminea*)	GSF	3	282	1217	22	328	680	528	160.43	80.06				
UCIAMS	186408	plant fragment	GSF	15	224	130	20	11	268	107	105.40	80.06	169.00	Y	Y	Anomalously young age; likely contamination or a root
YAUT	26733	stems/roots and one piece charcoal mud break in GSF	MF-U/GSF	15	123	19	39	-6	255	80	126.40	74.07	270.00			CALIBOMB, approximate median age: 1695 to 1956, most probably 1867 to 1918
UCIAMS	115624	charcoal	MF-U	15	69	5170	20	5902	5990	5927	72.40	74.07	324.00	Y	Y	Removed, out of stratigraphic order within core; very small fragment likely reworked
UCIAMS	115623	charcoal and insect parts	MF-U	15	40	180	20	1	289	185	43.40	74.07	353.00			Suspect age, out of stratigraphic order within core; multiple types of sample combined
UCIAMS	186403	stem/roots/charcoal within mud lens in GSF	MF-U/GSF	15	123	130	20	11	268	107	126.40	74.07	270.00			Suspect age, possible root age
UCIAMS	186404	wood in MF at base of GSF	MF-L	15	399	1255	20	1087	1276	1224	402.40	74.07	-6.00			
UCIAMS	169345	plant stem	MF-U	16	117	1040	15	926	957	942	102.13	75.51				

UCIAMS	169346	single charcoal fragment	MF-U	16	151	1510	20	1347	1408	1379	136.13	75.51				
UCIAMS	169347	plant stem	MF-U	16	310	1850	15	1713	1821	1747	295.13	75.51				
UCIAMS	169348	*Cerithidea californica*	MF-U	16	322	2220	15	1250	2010	1612	307.13	75.51				
UCIAMS	169349	multiple charcoal pieces	MF-U	16	168	1405	15	1292	1345	1307	153.13	75.51				
UCIAMS	153252	charcoal	MF-L	19	370	2160	20	2057	2301	2148	346.33	75.51	-9.00			
UCIAMS	153268	charcoal	MF-L	19	384	2180	15	2120	2302	2252	360.33	75.51	-23.00			
UCIAMS	186405	plant fragment 15 cm above top of GSF in MF	MF-U	19	129	830	30	683	783	727	105.33	75.51	232.00			
UCIAMS	186406	stem, plants growing up from MF to WSF at base of WSF	MF-U/WSF	19	67	225	20	9	307	199	43.33	75.51	294.00			
UCIAMS	186401	plant fragment	GSF	20	225	1395	15	1288	1343	1302	88.22	81.40	142.00			Suspect age; mottling indicates bioturbation
YAUT	26706	articulated ridged bivalve (*Chione undulata*)	GSF	20	265	1481	26	559	938	754	128.22	81.40	102.00			
YAUT	26725	articulated ridged bivalve (*Chione undulata*)	GSF	20	270	1429	47	520	909	707	133.22	81.40	97.00			
UCIAMS	115625	charcoal	MF-U	20	59	255	20	154	422	300	44.22	75.51	308.00			
UCIAMS	115626	insect parts	MF-U	20	86	185	20	1	289	185	71.22	75.51	281.00			
UCIAMS	153253	plant part	MF-L	20	380	2970	110	2856	3388	3134	365.22	75.51	-13.00			
UCIAMS	186402	plant fragment	MF-L	20	373	2240	15	2156	2332	2220	358.22	75.51	-6.00			
UCIAMS	186407	plant fragment	MF-U	20	110	660	15	562	665	586	95.22	75.51	257.00			

UCIAMS	186289	*Cerithidea californica* in lower GSF just above MF contact; within a mud clast	GSF	21	388	1835	15	829	1549	1193	253.05	81.40	6.00			Suspect age, Cerithidea californica within mud clast: reworked
YAUT	26735	root in mud clast between GSF upper and lower	MF-U/GSF	21	272	510	50	481	642	535	259.05	75.51	122.00			Suspect age, possible root age
UCIAMS	153254	plant part	MF-L	21	400	1915	20	1743	1885	1829	387.05	75.51	-6.00			
YAUT	26705	articulated thin bivalve (*Macoma nasuta*)	GSF	22	163	1426	29	528	899	703	36.53	81.40				
YAUT	26737	wood, not burnt	MF-U	25	100	205	22	1	300	182	92.76	75.51				
UCIAMS	169363	oyster shell (*Ostrea* spp.)	GSF	31	90	1625	15	683	1094	888	5.75	81.40				
YAUT	26736	plant part in GSF	GSF	41	233	1819	27	1624	1820	1719	239.70	80.56	52.00		Y	Suspect age, mottle indicates bioturbation; Out of stratigraphic order in OxCal compilation
UCIAMS	169360	limpet	GSF	41	273	4090	15	3543	4059	3789	279.70	80.56	12.00	Y	Y	Suspect age, out of stratigraphic order within core; mottling indicates bioturbation
UCIAMS	169361	plant stem	MF-L	41	287	2275	15	2181	2343	2321	415.70	74.60	-2.00			
UCIAMS	169362	plant parts	GSF	41	95	590	20	544	643	606	101.70	80.56	190.00			
UCIAMS	169341	*Cerithidea californica*	MF-U/BSF	43	121	1200	15	279	908	586	189.30	74.11				Suspect age, out of stratigraphic order within core; Cerithidea in sand bed, indicating reworking
UCIAMS	169339	plant stem	MF-U/BSF	43	85	885	15	732	897	769	153.30	74.11				
UCIAMS	169340	plant stem	MF-U/BSF	43	94	785	15	677	725	701	162.30	74.11				

UCIAMS	169342	multiple plant parts	MF-U/BSF	43	274	885	15	732	897	769	342.30	74.11				
UCIAMS	169343	partially burned stem	MF-U/BSF/GSF	43	275	835	15	688	773	730	221.30	80.10				
UCIAMS	169344	plant stem	GSF	43	281	1350	20	1179	1303	1288	227.30	80.10				
UCIAMS	186426	plant fragment	GSF	44	266	1560	15	1385	1516	1458	231.30	80.14	109.00	Y	Y	Removed, out of stratigraphic order within core; mottling indicates bioturbation
UCIAMS	186427	plant fragment	GSF	44	320	1445	15	1303	1354	1329	285.30	80.14	55.00	Y	Y	Removed, out of stratigraphic order within core; mottling indicates bioturbation
UCIAMS	186428	plant fragment	GSF	44	377	1590	15	1411	1521	1469	342.30	80.14	-2.00	Y	Y	Removed, out of stratigraphic order within core; mottling indicates bioturbation
UCIAMS	186424	woody charcoal in MF	MF-U	44	137	1465	30	1302	1388	1345	224.30	74.16	238.00	Y	Y	Removed, out of stratigraphic order within core; very small sample size
UCIAMS	186425	plant fragment	GSF	44	169	910	20	737	907	834	134.30	80.14	206.00			
UCIAMS	186429	plant fragment	MF-L	44	395	1200	15	1067	1176	1114	482.30	74.16	-20.00			
UCIAMS	129078	*Cerithidea californica*	MF-L/BSF	46	1130	5240	20	4924	5736	5360	1050.11	75.51	-578.00			Previously published in Simms et al., 2016
UCIAMS	129079	*Cerithidea californica*	MF-L/BSF	46	1224	5730	25	5545	6273	5899	1144.11	75.51	-672.00			Previously published in Simms et al., 2016
UCIAMS	129080	*Cerithidea californica*	MF-L/BSF	46	789	4020	20	3387	4256	3816	709.11	75.51	-237.00			Previously published in Simms et al., 2016

UCIAMS	129081	*Cerithidea californica*	MF-L/BSF	46	904	4520	20	4000	4877	4472	824.11	75.51	-352.00			Previously published in Simms et al., 2016
UCIAMS	151214	*Cerithidea californica*	MF-L	46	551	1865	20	873	1599	1225	471.11	75.51	0.00			sample at contact
YAUT	26708	*Cerithidea californica*	MF-L/BSF	46	755	4038	26	3407	4284	3839	675.11	75.51	-203.00			
YAUT	26709	*Cerithidea californica*	MF-L/BSF	46	959	4793	30	4400	5274	4821	879.11	75.51	-407.00			
YAUT	26711	*Cerithidea californica*	MF-L/BSF	46	1239	6047	38	5868	6632	6237	1159.11	75.51	-687.00			
YAUT	26712	*Cerithidea californica*	MF-L/BSF	46	745	3737	30	3025	3894	3462	665.11	75.51	-193.00			
YAUT	26713	*Cerithidea californica*	MF-L/BSF	46	750	3940	26	3297	4162	3714	670.11	75.51	-198.00			
YAUT	26716	*Cerithidea californica*	MF-L/BSF	46	907	4455	33	3941	4823	4386	827.11	75.51	-355.00			
YAUT	26717	*Cerithidea californica*	MF-L/BSF	46	959	4838	37	4434	5304	4882	879.11	75.51	-407.00			
YAUT	26718	*Cerithidea californica*	MF-L/BSF	46	1207	5866	28	5653	6399	6045	1127.11	75.51	-655.00			
YAUT	26719	*Cerithidea californica*	MF-L/BSF	46	1239	5929	34	5722	6482	6109	1159.11	75.51	-687.00			
YAUT	26722	*Cerithidea californica*	MF-L/BSF	46	882	4315	44	3733	4666	4202	802.11	75.51	-330.00			
UCIAMS	129084	charcoal	MF-L/BSF	46	1130	4645	20	5314	5461	5413	1050.11	75.51	-578.00			
UCIAMS	129085	charcoal	MF-L/BSF	46	1224	5295	20	5995	6184	6083	1144.11	75.51	-672.00			
UCIAMS	129086	charcoal	MF-L/BSF	46	789	3615	20	3848	3980	3923	709.11	75.51	-237.00			
UCIAMS	129087	charcoal	MF-L/BSF	46	904	3845	20	4152	4403	4252	824.11	75.51	-352.00			
UCIAMS	129088	charcoal	GSF	46	1369	5850	20	6569	6740	6671	1167.11	81.40	-817.00			
UCIAMS	129089	plant fragment	GSF	46	1363	5920	25	6667	6826	6738	1161.11	81.40	-811.00			
UCIAMS	151182	stem or wood part	MF-L	46	568	2730	20	2769	2863	2815	488.11	75.51	-16.00			
UCIAMS	151183	charcoal	MF-L/BSF	46	753	3305	20	3466	3567	3522	673.11	75.51	-201.00			
UCIAMS	151184	plant fragment	MF-L/BSF	46	807	3785	25	4085	4244	4163	727.11	75.51	-255.00			
UCIAMS	151185	charcoal	GSF/BSF	49	521	2035	25	1889	2052	1970	321.04	81.40				
UCIAMS	151186	seed	MF-L/BSF	49	654	3015	20	3083	3331	3209	576.04	75.51				
UCIAMS	151187	plant fragment	MF-L/BSF	49	687	3445	20	3637	3825	3703	609.04	75.51				
UCIAMS	151188	charcoal	MF-L/BSF	49	828	3960	100	4095	4811	4413	750.04	75.51				

UCIAMS	151189	charcoal	MF-L/BSF	49	1090	4560	60	4980	5457	5194	1012.04	75.51				
UCIAMS	151190	charcoal	MF-L/BSF	49	1256	5320	25	5999	6193	6085	1178.04	75.51				
UCIAMS	151191	charcoal	GSF	49	1407	5910	100	6488	6988	6736	1207.04	81.40				
UCIAMS	151192	charcoal	GSF	49	1460	5800	90	6398	6833	6600	1260.04	81.40				
UCIAMS	151215	*Cerithidea californica*	MF-L/BSF	49	928	4430	20	3920	4800	4353	850.04	75.51				
UCIAMS	153269	charcoal	MF-L/BSF	49	667	3000	20	3077	3324	3189	589.04	75.51				
UCIAMS	153236	plant fragment	MF-L/BSF	50	1239	5190	20	5910	5993	5944	1133.00	75.51				
UCIAMS	153248	plant fragment	MF-L/BSF	50	729	3240	20	3395	3483	3450	623.00	75.51				
UCIAMS	153249	charcoal	MF-L/BSF	50	1352	5385	25	6015	6282	6211	1246.00	75.51				
UCIAMS	153250	charcoal	MF-L/BSF	50	1239	5135	20	5759	5980	5908	1133.00	75.51				
UCIAMS	153251	charcoal	MF-L/BSF	50	667	3000	20	3077	3324	3189	561.00	75.51				
UCIAMS	151193	plant fragment	MF-U/BSF	51	363	845	20	690	785	742	257.00	75.51				
UCIAMS	151194	plant fragment	MF-L/BSF	51	663	3130	20	3257	3439	3360	557.00	75.51				
UCIAMS	151195	charcoal	MF-L/BSF	51	718	3325	30	3460	3635	3534	612.00	75.51				
UCIAMS	151196	charcoal-single piece, fragmented	MF-L/BSF	51	715	3210	20	3381	3456	3421	609.00	75.51				
UCIAMS	151197	plant fragment	MF-L/BSF	51	777	3365	45	3467	3811	3597	671.00	75.51				
UCIAMS	151198	plant fragment	MF-L/BSF	51	899	3765	25	3998	4235	4126	793.00	75.51				
UCIAMS	151199	plant fragment	MF-L/BSF	51	1079	4335	20	4849	4960	4883	973.00	75.51				
UCIAMS	151200	plant fragment	MF-L/BSF	51	1205	4595	25	5141	5445	5317	1099.00	75.51				
UCIAMS	151201	plant fragment	MF-L/BSF	51	1307	5235	20	5927	6165	5970	1201.00	75.51				